Disruption of TUFT1, a Desmosome-Associated Protein, Causes Skin Fragility, Woolly Hair, and Palmoplantar Keratoderma

JIDOpen

Annemieke J.M.H. Verkerk[1,14], Daniela Andrei[2,14], Mathilde C.S.C. Vermeer[3], Duco Kramer[2], Marloes Schouten[3], Pascal Arp[1], Joost A.M. Verlouw[1], Hendri H. Pas[2], Hillegonda J. Meijer[2], Marije van der Molen[2], Silke Oberdorf-Maass[3], Miranda Nijenhuis[2], Pedro H. Romero-Herrera[3], Martijn F. Hoes[3], Jeroen Bremer[2], Johan A. Slotman[4], Peter C. van den Akker[5], Gilles F.H. Diercks[6], Ben N.G. Giepmans[7], Hans Stoop[8], Jasper J. Saris[9], Ans M.W. van den Ouweland[9], Rob Willemsen[9], Jean-Jacques Hublin[10,11], M.Christopher Dean[12,13], A.Jeannette M. Hoogeboom[9], Herman H.W. Silljé[3], André G. Uitterlinden[1], Peter van der Meer[3] and Maria C. Bolling[2]

Desmosomes are dynamic complex protein structures involved in cellular adhesion. Disruption of these structures by loss-of-function variants in desmosomal genes leads to a variety of skin- and heart-related phenotypes. In this study, we report TUFT1 as a desmosome-associated protein, implicated in epidermal integrity. In two siblings with mild skin fragility, woolly hair, and mild palmoplantar keratoderma but without a cardiac phenotype, we identified a homozygous splice-site variant in the *TUFT1* gene, leading to aberrant mRNA splicing and loss of TUFT1 protein. Patients' skin and keratinocytes showed acantholysis, perinuclear retraction of intermediate filaments, and reduced mechanical stress resistance. Immunolabeling and transfection studies showed that TUFT1 is positioned within the desmosome and that its location is dependent on the presence of the desmoplakin carboxy-terminal tail. A *Tuft1*-knockout mouse model mimicked the patients' phenotypes. Altogether, this study reveals TUFT1 as a desmosome-associated protein, whose absence causes skin fragility, woolly hair, and palmoplantar keratoderma.

Journal of Investigative Dermatology (2023) ■, ■−■; doi:10.1016/j.jid.2023.02.044

[1]*Department of Internal Medicine, Erasmus University Medical Center, Rotterdam, The Netherlands;* [2]*Department of Dermatology, University of Groningen, University Medical Centre Groningen, Center of Expertise for Blistering Diseases, Groningen, The Netherlands;* [3]*Department of Cardiology, University Medical Center Groningen, University of Groningen, Groningen, The Netherlands;* [4]*Optical Imaging Centre, Erasmus University Medical Center, Rotterdam, The Netherlands;* [5]*Department of Genetics, University of Groningen, University Medical Centre Groningen, Center of Expertise for Blistering Diseases, Groningen, The Netherlands;* [6]*Department of Pathology and Medical Biology, University Medical Center Groningen, University of Groningen, Groningen, The Netherlands;* [7]*Department of Biomedical Sciences of Cells & Systems, University Medical Centre Groningen, University of Groningen, Groningen, The Netherlands;* [8]*Department of Pathology, Erasmus University Medical Center, Rotterdam, The Netherlands;* [9]*Department of Clinical Genetics, Erasmus University Medical Center, Rotterdam, The Netherlands;* [10]*Department of Human Evolution, Max Planck Institute for Evolutionary Anthropology, Leipzig, Germany;* [11]*Chaire de Paléoanthropologie, CIRB (UMR 7241 − U1050), Collège de France, Paris, France;* [12]*Centre for Human Origins Research, Natural History Museum, London, United Kingdom; and* [13]*Department of Cell and Developmental Biology, University College London, London, United Kingdom*

[14]*These authors contributed equally to this work.*

Correspondence: Annemieke J.M.H. Verkerk. Erasmus Medical Center Rotterdam, Department of Internal Medicine, Rotterdam, The Netherlands. E-mail: j.verkerk@erasmusmc.nl or Maria C. Bolling, University of Groningen, University Medical Center Groningen, Department of Dermatology, Center of Expertise for Blistering Diseases, Groningen, The Netherlands. E-mail: m.c.bolling@umcg.nl

Abbreviations: DSG, desmoglein; DSP, desmoplakin; IF, intermediate filament; K, keratin; KC, keratinocyte; KO, knockout; WH, woolly hair; WT, wild-type

Received 14 February 2023; accepted 24 June 2023; accepted manuscript published online XXX; corrected proof published online XXX

INTRODUCTION

The epidermis is the outermost skin layer, which is remarkably resistant to high levels of mechanical stress. An important complex to support the strength and flexibility of the epidermal cell−cell contact is the desmosome, a dynamic structure with critical adhesive functions, whose components are regulated during tissue remodeling and differentiation (Nekrasova and Green, 2013). This structure is a spot weld site that confers robust intercellular cohesion through the anchorage of intermediate filaments (IFs) to the plasma membrane. Since the discovery of the fundamental structure of desmosomes >60 years ago (Obland, 1958), various studies contributed to discovering their components, belonging to three major protein families: cadherins (desmogleins [DSGs]1−4, DSC1−3), armadillo proteins (plakoglobin, PKP1−3), and plakins (desmoplakin [DSP], plectin) (Green and Simpson, 2007; Lee and McGrath, 2021). In the skin, the desmosomes are connected to each other and with the nucleus by a network of circumferential and radial IFs composed of different keratins (Quinlan et al., 2017).

Disease-associated variants in genes encoding desmosomal proteins or their regulators can cause peeling, erosive, or blistering skin disorders as well as nonsyndromic woolly hair (WH) or palmoplantar keratoderma (Najor, 2018; Vermeer et al., 2022). Desmosomes also have an important function in the heart, reflected by loss-of-function variants in *DSP* (McKoy et al., 2000; Norgett et al., 2000), the plakoglobin gene *JUP* (McKoy et al., 2000; Norgett et al., 2000),

and *DSC2* (Beffagna et al., 2007; Gehmlich et al., 2011), which can cause nonsyndromic cardiomyopathy and cardiocutaneous syndromes (Vermeer et al., 2022). In recent years, significant progress has been made in the identification and characterization of different genes involved in skin fragility and related disorders; however, approximately 15% of the cases remain genetically unsolved (Has et al., 2020; Takeichi et al., 2015).

In this study, we have identified and characterized the desmosome-associated protein Tuftelin 1 (TUFT1) (encoded by the gene *TUFT1*), loss of which causes desmosomal dysfunction with skin fragility, WH, and palmoplantar keratoderma in humans and mice. Previously, TUFT1 was linked to processes such as enamel mineralization (Deutsch et al., 1991), chondrogenesis (Sliz et al., 2017), and tumorigenesis (Deutsch et al., 1991; Sliz et al., 2017; Zhou et al., 2016). Very recently, biallelic loss-of-function variants in *TUFT1* have been associated with a peeling skin phenotype with WH in three pedigrees (Jackson et al., 2023). In this study, we present an additional two siblings with a similar phenotype and provide functional data, including from a *Tuft1*-knockout (KO) mouse model, which designate TUFT1 as a desmosome-associated protein that plays a critical role in cell–cell adhesion and skin and hair morphogenesis.

RESULTS

Skin fragility, WH, and focal palmoplantar keratoderma observed in two Dutch siblings

Upon clinical investigation, two children, born to healthy parents from a small Dutch family of Caucasian ancestry, were diagnosed with skin fragility, WH, and focal palmoplantar keratoderma (Figure 1).

Both affected children had light-colored, tightly curled scalp hair; eyelashes (Figure 1a, b, and f); eyebrows; and body hairs. The skin fragility was mild, with focal erosions resembling peeling of the skin and occasionally vesicles/blisters upon everyday mechanical traumas (Figure 1b–d and h), and was more prevalent in summer than in winter. Mild focal palmoplantar keratoderma and extensive keratosis pilaris were seen (Figure 1e, g, i, and j). The teeth were all present and had a normal appearance, although both affected persons reportedly had a higher tendency to caries than the unaffected family members. Cardiological examination did not reveal any apparent abnormalities on electrocardiogram

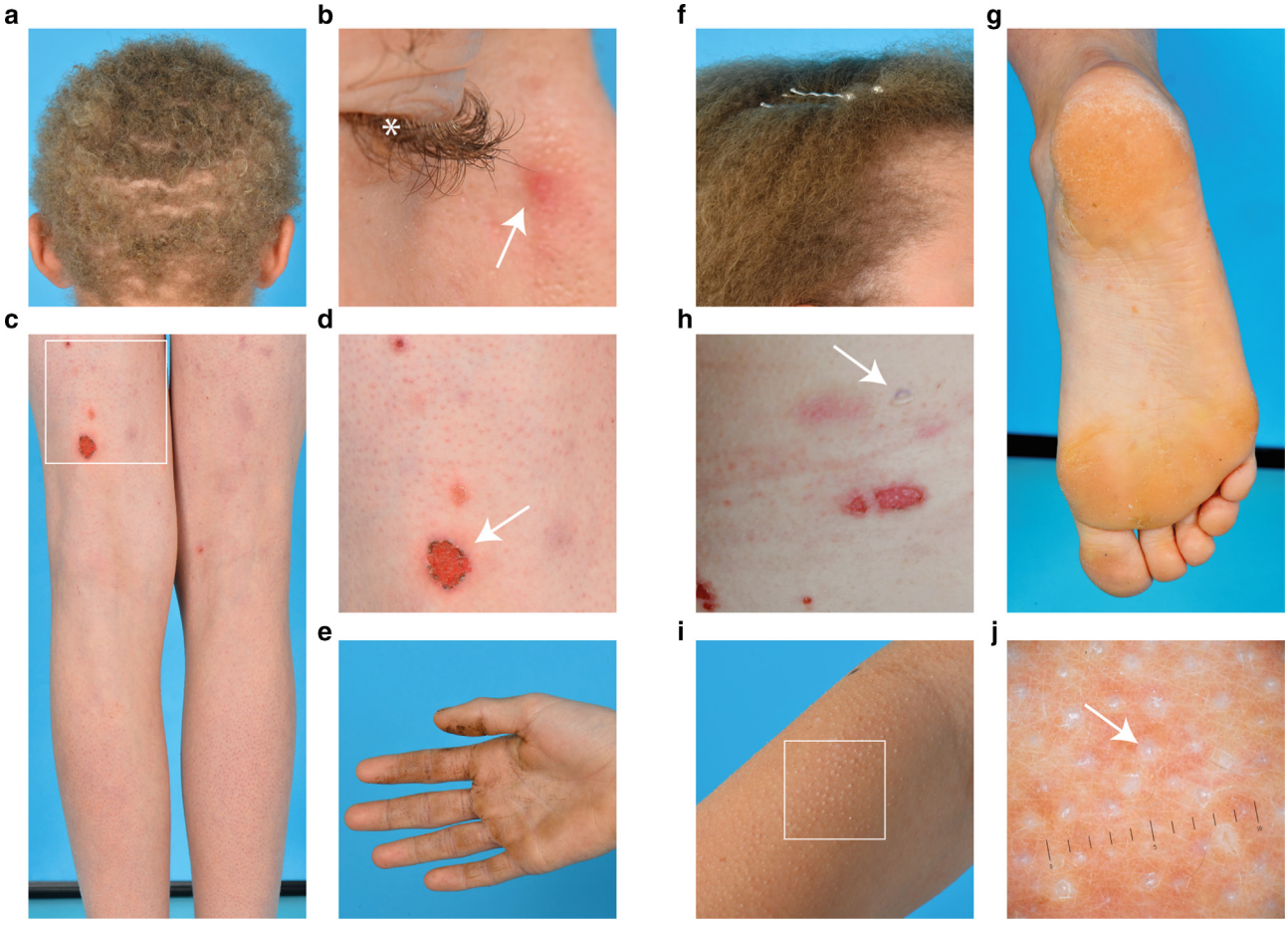

Figure 1. Clinical phenotype of the two affected children. (**a**–**e**) Male and (**f**–**j**) female. Images of **a** the boy's woolly hair, including some bald spots at the age of 15 years; (**b**) curly eyelashes (asterisk) and mild erosions induced by wearing glasses (arrow); (**c, d**) mild skin fragility showing superficial erosions without severe blistering (arrow)—**d** is zoom-in of **c**; and (**e**) palmar hyperkeratosis. Images of (**f**) the girl's woolly hair, (**g**) hyperkeratosis on the soles of the feet, (**h**) mild skin erosions and a vesicle upon skin rubbing (arrow), and (**i**) keratosis pilaris; **j** is a microscopic image of **i** revealing the small hyperkeratotic plugs (arrow). Written informed consent was obtained from the parents for publication of the images.

or ultrasound at different time points during clinical follow-up (last time points were at ages 17 and 19 years).

A homozygous splice variant in the *TUFT1* gene leads to alternative splicing with a frameshift and premature termination codon

SNP array analysis on the DNA of the two patients identified several homozygous regions (Supplementary Table S1), suggesting consanguinity of the parents. Variant filtering of whole exome sequencing data of the two patients and their father, assuming recessive inheritance (Figure 2a and Supplementary Table S2), combined with a selection of variants residing in the identified homozygous areas, identified a homozygous splice acceptor site variant in intron 8, c.724-2A>G (chr1:151.547.385, build 37, NM_020127.2; ENST00000368849), of the *TUFT1* gene in the two affected children, whereas the father was a heterozygous carrier for this variant. Sanger sequencing validation confirmed these findings and, in addition, showed the mother to be a heterozygous carrier as well (Figure 2b). Splice site analysis programs (Alamut, version 2.7.2, SOPHiA Genetics, Lausanne, Switzerland) predicted skipping of exon 9 to be the most likely outcome, and given the 100% evolutionary conserved sequence

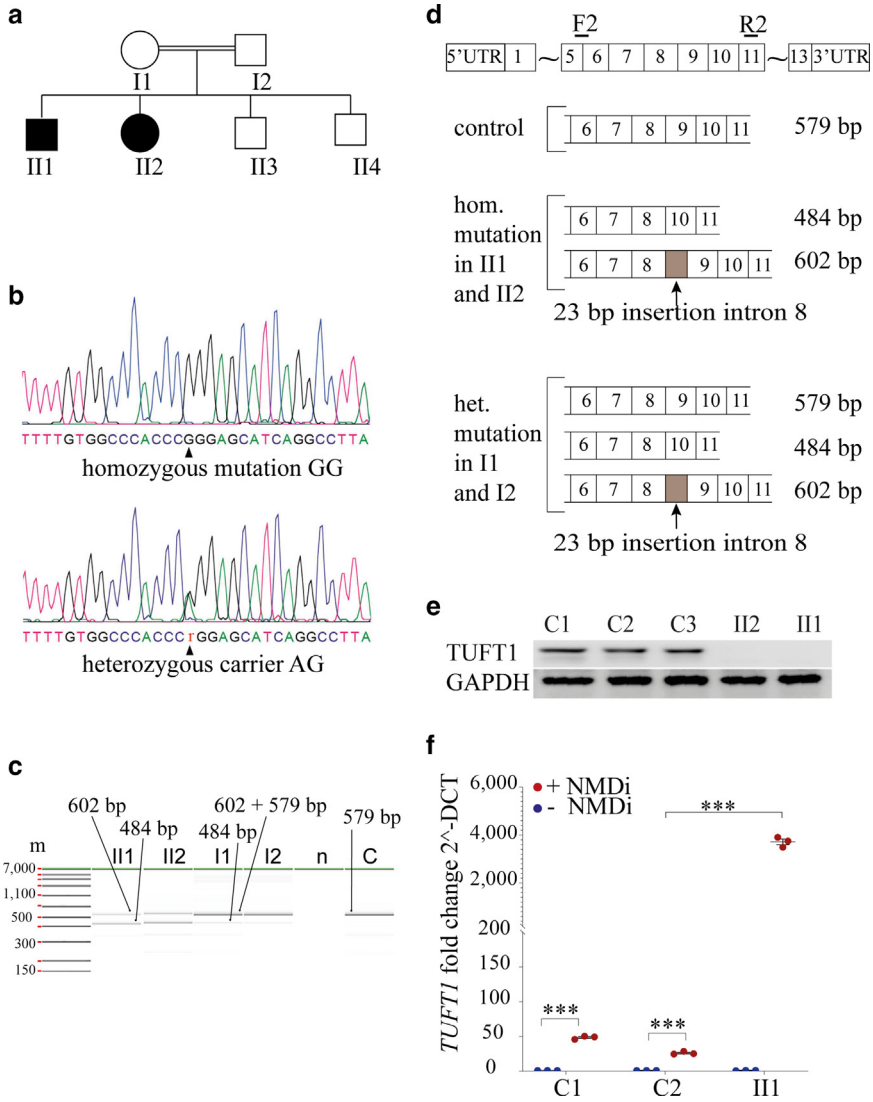

Figure 2. Genetic analysis of the patients. (**a**) Pedigree of the family. Filled symbols represent affected individuals, and empty symbols represent healthy family members. The double line represents the consanguinity of the parents. (**b**) DNA Sanger sequence validation showing the *TUFT1* splice mutation in intron 8 (c.724-2A>G). The normal sequence from intron 8 to exon 9 is acccagGAGCAT, with the last six bases of intron 8 indicated in lowercase letters and the first six bases of exon 9 in capital letters. The position of the mutation a>g is underscored. Homozygous mutation as seen in probands II1 and II2 (top panel) and heterozygous mutation in carrier parents I1 and I2 (lower panel) are indicated by an arrowhead. (**c**) Electrophoretic analysis (labchip) shows RT-PCR products on lymphocyte RNA of patients II1 and II2, heterozygous carrier parents I1 and I2, and control (denoted as C). n = negative control without DNA. M = HT DNA HiSens ladder (PerkinElmer, Waltham, MA). (**d**) Schematic view of *TUFT1* cDNA products identified in the family members after sequencing of the different RT-PCR products. Exon numbers are indicated. (**e**) Keratinocyte protein extracts tested by western blot. Patients II1 and II2 protein quantification by western blot shows a complete absence of TUFT1 protein. C1, C2, and C3 are different donor controls. Antibodies are listed in Supplementary Table S5. (**f**) Effect of NMDi on relative *TUFT1* mRNA expression levels in control and patient fibroblasts. After NMDi treatment, expression levels of mutated *TUFT1* transcripts in the patient increased 3,700 times fold compared with *TUFT1* transcript levels in controls with 26 times and 48 times fold increase; average Ct values: C1 = 29.8, C1 + NMDi = 24.2, C2 = 27.9, C2 + NMDi = 23.2, II1 = 36.2, and II1 + NMDi = 23.9. Error bar = SEM, data were analyzed by paired *t*-test; ***$P < 0{,}0005$. hom. denotes homogenous; het. denotes heterogenous. UTR, untranslated region; NMDi, nonsense-mediated mRNA decay inhibition.

of the −2A splice acceptor site, this nucleotide change was expected to destroy the splice acceptor site of intron 8 (Zhang, 1998). This variant was not present in the gnomAD database (version 2.1.1) (Lek et al., 2016) or any other public population variant frequency database. None of the known genes involved in skin fragility and cardiocutaneous syndromes, as mentioned in Supplementary Table S3, were located in any of the identified homozygous regions nor revealed any variants indicative to be disease causing. RT-PCR was performed on lymphocyte mRNA from the patients and both parents and revealed alternative splicing leading to a frameshift and premature termination codon (Figure 2c and d and Supplementary Figure S1a). Because aberrant splicing of exon 9 was predicted (Alamut, version 2.7.2), primers were designed on exon 5/6 and exon 11 to produce RT-PCR fragments. In a normal control, this produced a 579-bp fragment as calculated. With the predicted skipping of exon 9, a 95-bp shorter fragment (484 bp) was expected and was indeed observed in the affected children. However, also, a larger fragment (602 bp) was present. With Sanger sequencing, this fragment was shown to contain 23 bp from intron 8 plus the complete exon 9. Owing to the loss of the original splice nucleotide, in addition, an alternative splice acceptor site (AG) in intron 8 was used (Supplementary Figure S1a), retaining 23 bases from intron 8, as well as exon 9 in this fragment. On the basis of signal intensities, it was estimated that the alternative acceptor site was used in approximately 50% of the transcripts, retaining 23 bases from intron 8 and including exon 9, and in approximately 50% of the transcripts, exon 9 was skipped. No normal cDNA product was observed. The heterozygous parents each showed the normal 579 bp cDNA fragment and the aberrant 484/602 bp fragments. In a healthy control, only the 579 bp transcript with the normal exon 9 sequence was found (Figure 2d). Hence, the identified splice-site variant leads to a frameshift and premature stop codon for both aberrant cDNA products.

Nonsense-mediated RNA decay leads to loss of TUFT1 protein

To determine the possible contribution of nonsense-mediated mRNA decay of mutated mRNA, we investigated the relative expression levels of *TUFT1* mRNA in cultured skin fibroblast cells from one patient and two age-matched controls. Cells were incubated with and without cycloheximide, a translation inhibitor that blocks nonsense-mediated mRNA decay (Noensie and Dietz, 2001; Schweingruber et al., 2013) (Figure 2f). A 3,700 times fold increase was observed in the patient *TUFT1* mRNA levels, in contrast with only 25 times and 48 times fold increase in the controls, indicating nonsense-mediated mRNA degradation for the mutated *TUFT1* transcript in the patients. Western blot of the patient's keratinocyte (KC) extract with a TUFT1 C-terminal antibody showed the absence of TUFT1 protein (Figure 2e). qPCR of *TUFT1* transcripts showed a strong reduction in the patient's KCs and fibroblasts (Supplementary Figure S2a and b).

Patient skin shows strongly reduced TUFT1 expression and structural abnormalities

H&E staining of perilesional skin biopsy sections from patient II1 showed mild acanthosis and spongiosis with marked intercellular widening with the tendency to acantholysis and a subcorneal split (Figure 3a). Immunofluorescent staining of TUFT1 on control human skin showed an epidermal cell membrane expression pattern and a strong reduction to near absence in the patient's skin (Figure 3b). The basement membrane zone staining in control and patient skin was nonspecific, as in *Tuft1*-KO mice, the epidermal cell membrane staining of this antibody (antibody N3C3) disappeared, but the basement membrane zone staining remained (Supplementary Figure S5b). Additional stainings for the basement membrane zone and other desmosomal proteins and different keratins on patient II1 skin biopsies did not indicate any reduction or upregulation (Supplementary Figure S3a). Electron microscopy of patient II1's skin biopsy revealed keratin IF detachment at the inner dense plaque of the desmosomes and their retraction toward the nucleus in thick, dense clusters (Figure 3c, lower panels).

Patients' KCs show structural abnormalities and weakened cell−cell contacts

Upon analyzing the morphology of the patients' cultured KCs on H&E, KCs from both patients (II1 and II2) showed significantly larger intercellular spaces than healthy control KCs (Figure 4a [upper panels] and b).

TUFT1 staining on control KCs showed a cell−cell border staining, resembling desmosomes-like dotted patterns in control cells, while being completely absent in patient cells (Figure 4a [middle panels] and c). In addition, DSP, a protein necessary to maintain desmosomal integrity (Vasioukhin et al., 2001), had a disturbed and more focal distribution along the cell borders in the patient cells (Supplementary Figure S3b). The IF keratin (K)5 showed a strong retraction in the proximity of the nucleus in patients' cells (Figure 4a, lower panels). The KC total protein quantification of the desmosomal/IF proteins by western blot analysis did not show any significant dysregulation (Supplementary Figure S3c).

Assessment of the in vitro intercellular adhesiveness of KCs through a KC dissociation assay, by subjecting detached KC monolayers to controlled mechanical stress through pipetting (Hartlieb et al., 2013; Simpson et al., 2010), showed extensive fragmentation of the patients' KC monolayer, compared with intact monolayers of control KCs. Altogether, these data underpin that TUFT1 is involved in desmosomal cell−cell contact (Figure 4d).

TUFT1 localizes at KC cell−cell borders, colocalizes with desmosomal proteins, and depends on DSP expression

Cotransfection of human KCs (HaCaT) with a GFP-labeled TUFT1 plasmid and either mCherry-DSG2 or mApple-K14 showed that TUFT1 colocalized at the plasma membrane with the desmosomal protein DSG2, which is mainly expressed in cultured KCs (Figure 5a, upper panels) and with IF K14 at the membrane insertion site (Figure 5a, lower panels). To accurately localize TUFT1 within the desmosome we performed superresolution microscopy (direct stochastic optical reconstruction microscopy) (Xu et al., 2017). TUFT1 flanked both the transmembrane protein DSG3 and the anchoring protein DSP on the intracellular side, and consequently, TUFT1 localized closest to the desmosomal IFs, at the inner dense plaque. Plaque-to-plaque distance measurements of DSP, as previously shown within a similar range as our current results (Stahley et al., 2016), are shown next to TUFT1 measurements, which show a slightly bigger

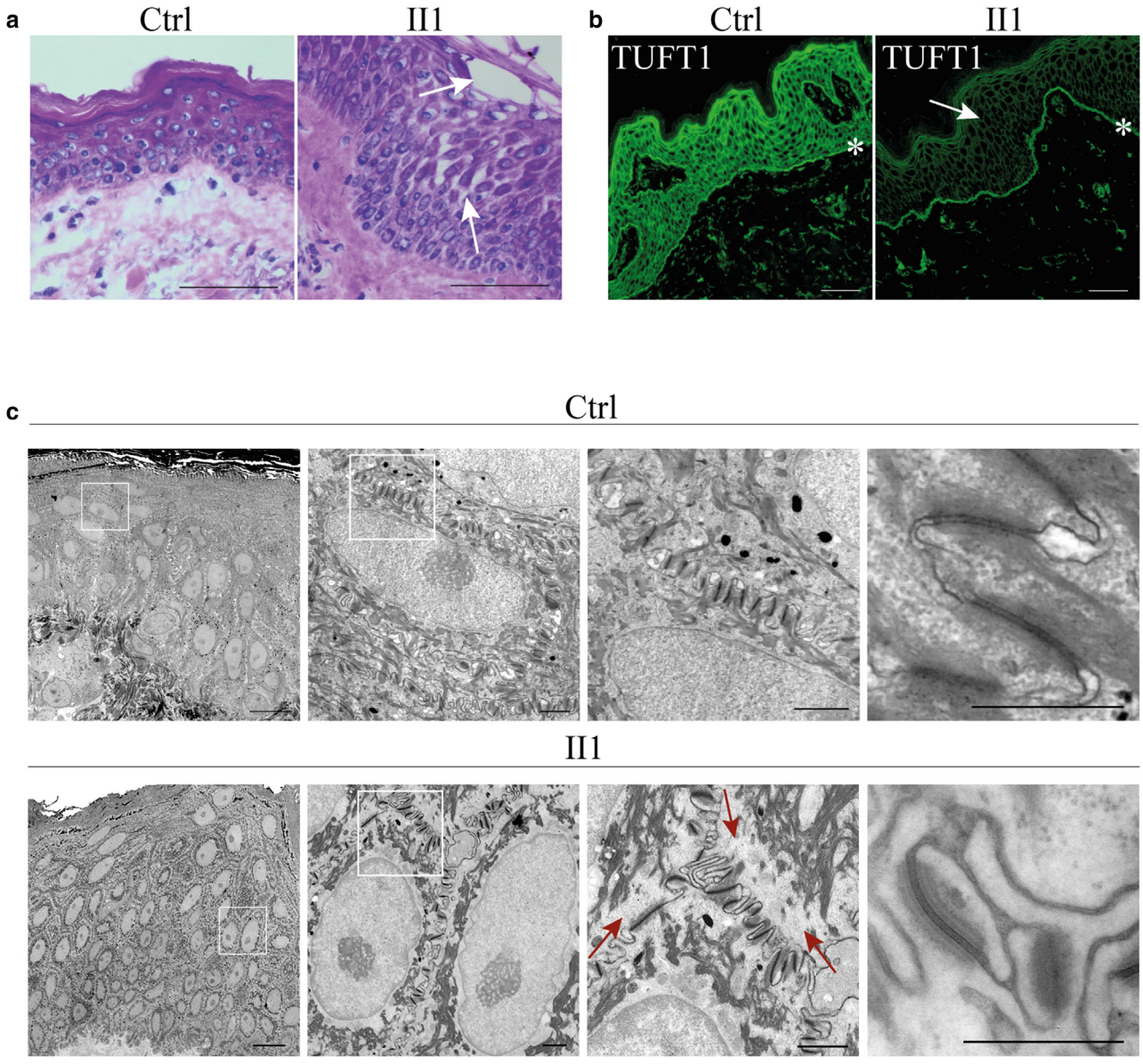

Figure 3. Patients' skin analysis. (**a**) Patient II1 skin biopsy analysis (H&E) staining shows mild acanthosis and a subcorneal split in the epidermis (upper arrow) with widened spaces between keratinocytes and mild acantholysis (lower arrow), compared with that of Ctrl. Bar = 50 μm. (**b**) Immunofluorescence microscopy of TUFT1 staining shows a marked reduction at the epidermal cell surface in patient II1 skin compared with that of Ctrl. Note the nonspecific basement membrane zone staining in the Ctrl and II1 (asterisk). Bar = 50 μm. Antibodies are listed in Supplementary Table S5. (**c**) Ultrastructural electron microscopy analysis of the skin shows perinuclear aggregation of intermediate filaments in patient II1 (lower panel, second image) with keratin intermediate filament disruption from the desmosome (lower panel, third image, red arrows). The patient's desmosome structures appear normal, with an inner-dense plaque and an outer-dense plaque (lower panel, fourth image). Boxes indicate regions of magnification. Bar = 10 μm for the left images, 1 μm for the second and third zoom images, and 500 nm for the fourth images. Ctrl, control.

median distance than DSP (Figure 5b). TUFT1 also closely colocalized with DSC3 and the IFs K14 and K6 (Supplementary Figure S4a). In addition, electron microscopy immunolabeling of TUFT1 on cultured primary KCs positioned TUFT1 on the cytoplasmic side of the desmosome at the inner dense plaque, corroborating the direct stochastic optical reconstruction microscopy results (Figure 5c). TUFT1 protein expression in culture conditions was dependent on calcium concentration (Supplementary Figure S4b), similar to what is known for other desmosomal proteins (Watt et al., 1984).

Furthermore, we investigated whether TUFT1 protein expression within the desmosome was dependent on the desmosomal components DSP (associated with severe skin fragility [Jonkman et al., 2005]) and PKP1 using available KO/mutated primary KC lines (Jonkman et al., 2005). In KCs from a patient with lethal acantholytic epidermolysis bullosa due to a compound heterozygous variant in *DSP* (*DSP*:c.6370delTT/c.6069C>T) causing a carboxyl-terminal truncation (Jonkman et al., 2005), TUFT1 failed to stain at the cell–cell border, whereas plakoglobin still did. This suggests that TUFT1 association within the desmosome is

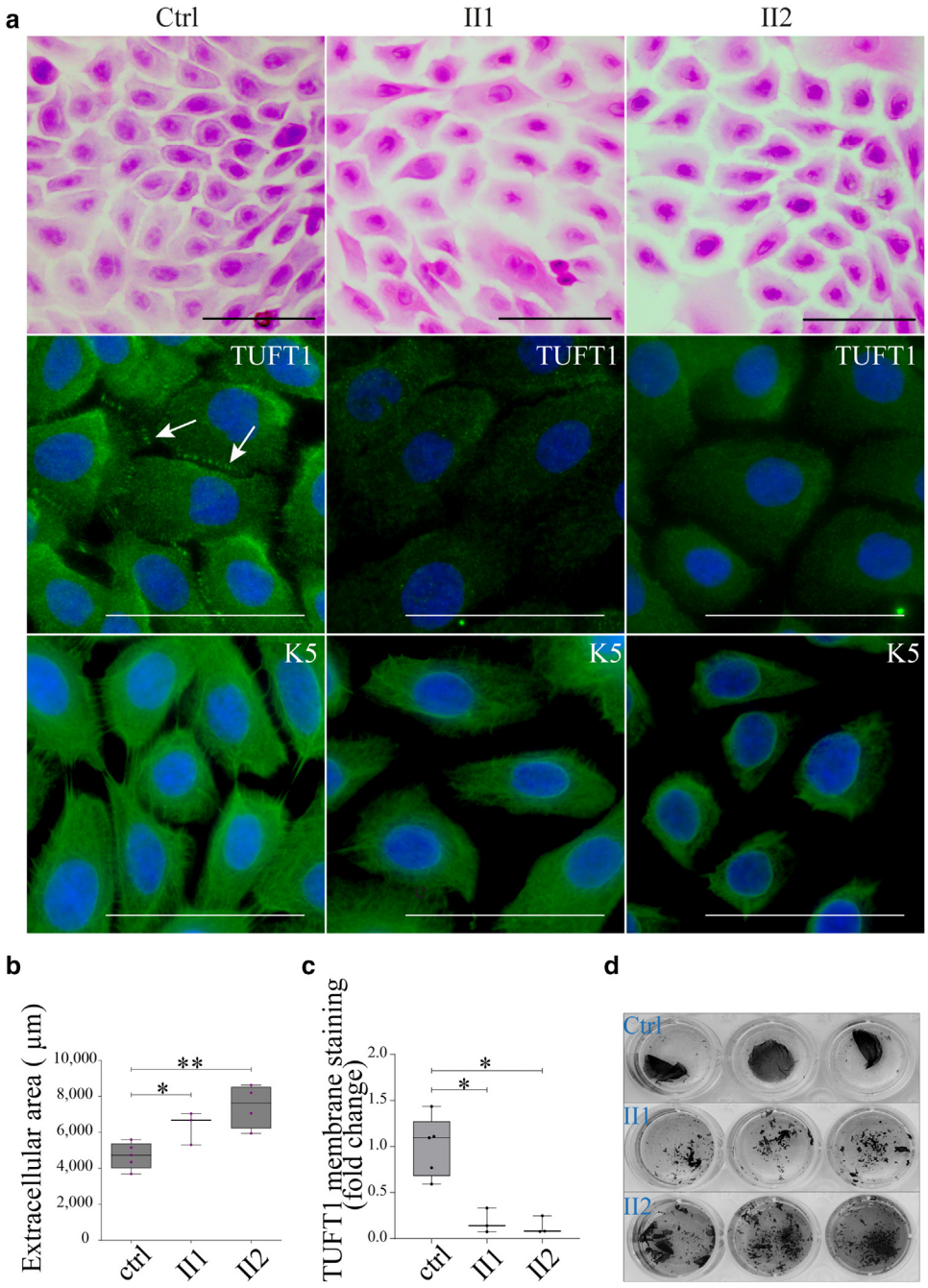

Figure 4. In vitro primary keratinocytes characterization. (**a**) Upper panels: H&E of cultured patient keratinocytes shows larger intercellular spaces than Ctrl cells. Bar = 50 µm. Middle panels: TUFT1 immunofluorescence staining of keratinocytes (green) shows a cell−cell border staining in Ctrl cells (arrows), whereas this is absent in the patients. Lower panels: Keratin 5 staining (green) shows a perinuclear retraction of the intermediate filaments. Nuclear staining was done with DAPI (blue). Bar = 50 µm. Antibodies are listed in Supplementary Table S5. (**b**) Quantification of the extracellular space shows that the area is significantly larger in both patients (ctrl represents five H&E images, II1 represents three, and II2 represents four H&E images). Error bar = SEM; data were analyzed by unpaired *t*-test. $^{**}P < 0.005$ and $^{*}P < 0.05$. (**c**) TUFT1 immunofluorescent intensity is quantified at the membrane; data were analyzed with Mann−Whitney test. $^{*}P < 0.05$. (**d**) KDA shows extensive disruption of the patients' II1 and II2 keratinocyte monolayers in comparison with those of Ctrl. Ctrl, control; KDA, keratinocyte dissociation assay.

DSP C-terminal dependent (Figure 5d). TUFT1 still localized at the cell−cell border in PKP1-deficient primary human KCs (homozygous *PKP1*: c.1680+1G>A [NM_001005337.3]) (Supplementary Figure S4c), indicating that TUFT1−DSP dependency is specific. However, this dependency is not mutual because DSP still localized at the cell membrane of *TUFT1*-mutated patients' cells, albeit in a different, more clustered-punctate pattern (Supplementary Figure S3b).

Tuft1-KO causes WH and spontaneous skin erosions in mice

Tuft1-deficient mice presented with a woolly/wavy hair phenotype (Figure 6a) (Brown and Moore, 2012) and groove-shaped hairs upon scanning electron microscopy analysis (Supplementary Figure S5a). Fourteen of 35 homozygous KO mice developed spontaneous skin fragility over time owing to grooming, scratching, and/or fighting compared with none of the wild-type (WT) mice (Figure 6c and d). Heterozygous mice did not show any hair or skin abnormalities. The first skin erosion outbursts in KO mice seemed to start a cascade of itching reactions that worsened the phenotype over time. Measures such as isolating affected mice or nail cutting did not improve animals welfare; thus, affected mice were killed owing to humane endpoints. H&E staining of the wounded skin showed a suprabasal split in the epidermis, with acantholysis and acanthosis (Figure 6e and f). TUFT1 immunofluorescence staining of the WT skin showed epidermal staining (Figure 6g) and was completely negative in KO mice

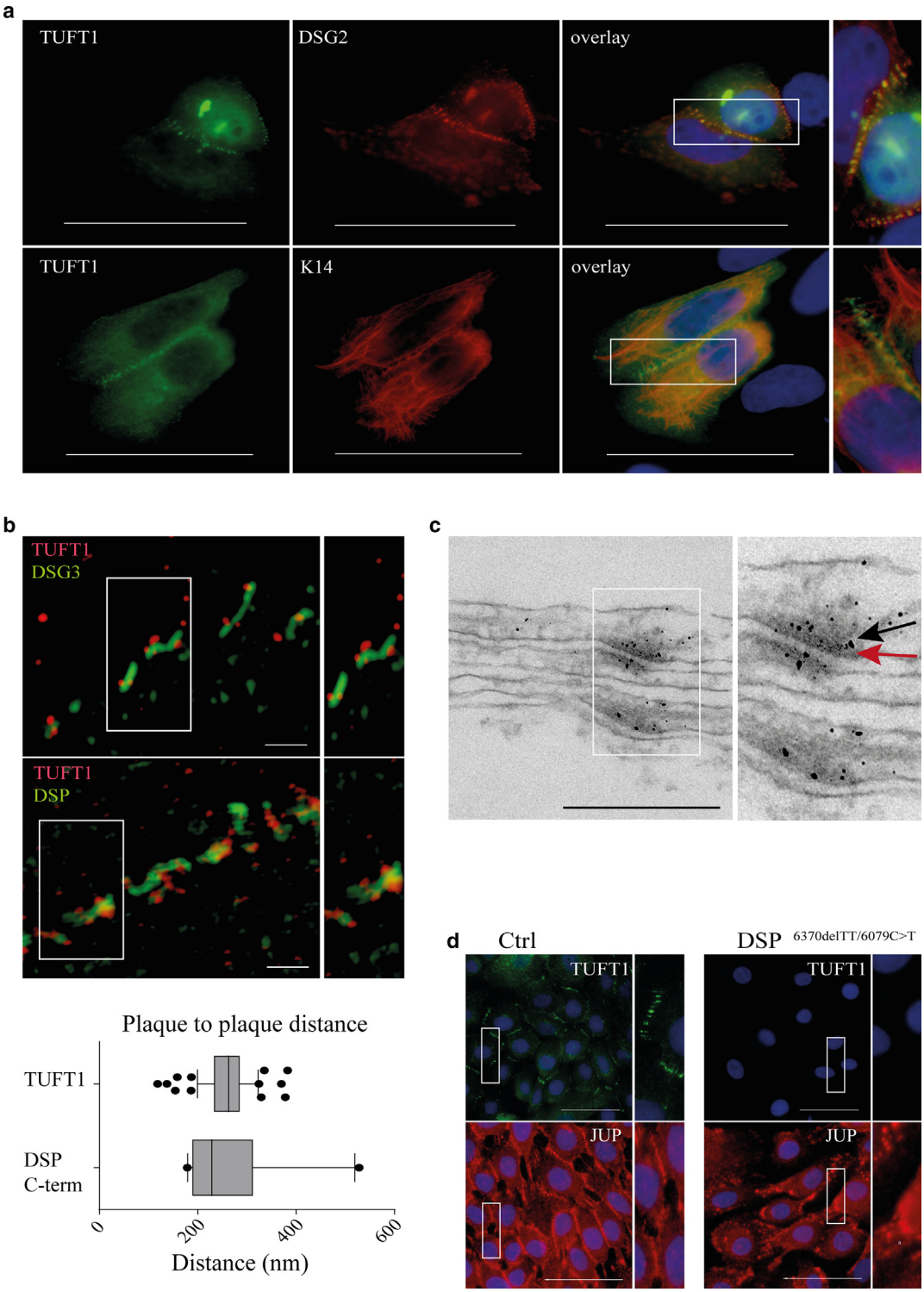

Figure 5. TUFT1 localization. (**a**) HaCaT cells cotransfected with TUFT1−GFP and DSG2−mCherry/K14−mApple shows colocalization of TUFT1 with the desmosomal proteins DSG2 at the plasma membrane (upper panels) and K14 intermediate filaments at the membrane insertion site (lower panels). Bar = 50 μm. (**b**) Immunofluorescence staining with antibodies against TUFT1 (red), DSG3 (green), and the DSP c-terminal (green) on primary human control keratinocytes analyzed through direct stochastic optical reconstruction microscopy imaging shows that TUFT1 flanks both DSG3 and DSP and localizes closest to DSP. Bar = 1 μm. Antibodies are listed in Supplementary Table S6. Plaque-to-plaque distance measurement in nanometers is shown in the box (25−75% box) and whiskers plots (10−90% whiskers). (**c**) TUFT1 immunolabeling on cultured control primary keratinocytes visualized by electron microscopy as gold nanoparticles (the white box indicates the magnified area on the right) shows localization of TUFT1 within the desmosome on the intracellular side. Black arrow = outer dense plaque; red arrow = inner dense plaque. Bar = 1 μm. Antibodies are listed in Supplementary Table S7. (**d**) Cultured C-terminal truncated DSP (compound heterozygous *DSP* mutation: c.6370delTT/c.6069C>T) primary keratinocytes fail to show a membrane TUFT1 staining as is seen in the control (upper panel). The *DSP*-mutated keratinocytes show remnants of desmosomes with JUP staining (lower panel). Magnified areas indicated with boxes are shown on the right. Bar = 50 μm. Antibodies are listed in Supplementary Table S5. C-term denotes C-termimal. DSG, desmoglein; DSP, desmoplakin; JUP, plakoglobin; K14, keratin 14.

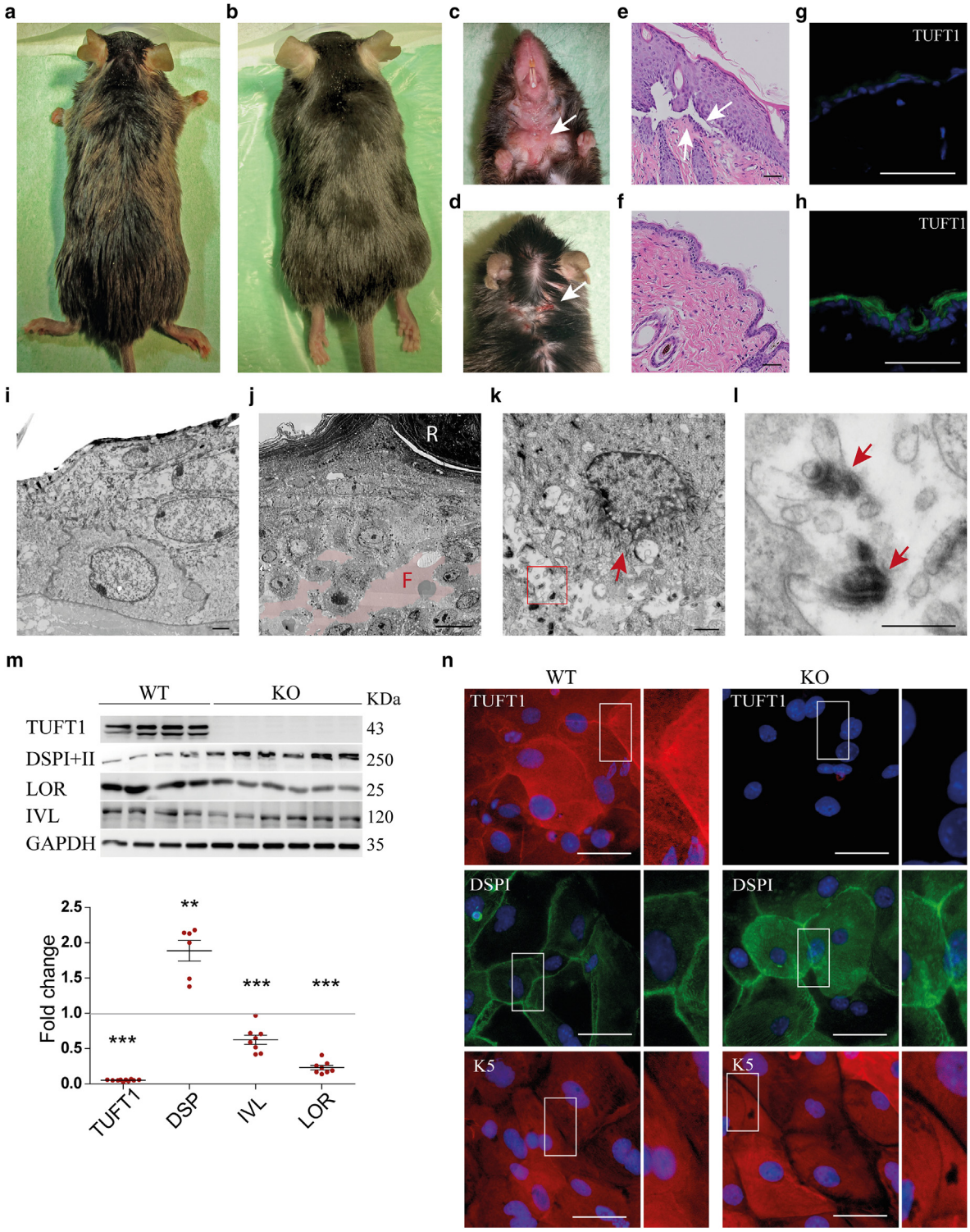

Figure 6. Mouse *Tuft1* KO characterization. (**a**) Woolly hair of homozygous *Tuft1*-KO mice and (**b**) straight hair of WT mice. (**c, d**) Wounds and erosions in KO mice. (**e**) Acanthosis and suprabasal epidermal split in lesional skin of KO mice (arrows) compared with (**f**) the epidermis of the WT mice. TUFT1 immunofluorescence staining shows (**g**) an epidermal pattern in WT skin (green) compared with (**h**) that of the KO skin, which is completely negative. Electron microscopy of (**i**) WT skin and (**j**) spontaneous blistered KO skin with blister fluid depicted in pink and with (**k**) bundles of keratin filaments in the proximity of the nucleus (arrow) and magnification in **l** of intact but free-floating desmosomes (arrows) without keratin attachment in the proximity of the blister fluid. F denotes blister fluid, and R denotes wound roof. Bar in **i** and **j** = 10 μm, in **k** = 1 μm, and in **l** = 500 nm. (**m**) Keratinocytes cultured from WT (n = 4) and KO (n = 6) mice aged 3 months analyzed by western blot for the indicated proteins: TUFT1, DSP, LOR, and IVL, indicating a downregulation of LOR and IVL and an upregulation of desmoplakin in the KO mice. Error bar = SEM; data were analyzed with unpaired *t*-test. $^{**}P < 0.005$ and $^{***}P < 0.0005$. (**n**) Immunofluorescence staining for TUFT1, DSP, and K5 shows an upregulation and accumulation of DSP predominantly in the cytoplasm of the KO cells and wider intercellular spaces for K5-stained KO keratinocytes. Bar = 50 μm. Antibodies are listed in Supplementary Table S5. BM, basement membrane; DSP, desmoplakin; IVL, involucrin; K5, keratin 5; KO, knockout; LOR, loricrin; WT, wild-type.

(Figure 6h). Immunofluorescent stainings of other desmosomal/hemidesmosomal proteins on mouse skin did not show significant differences (Supplementary Figure S5b).

On ultrastructural levels, the spontaneous wounds showed blister fluid under a thick scab roof (Figure 6j) and abnormal KCs with keratin bundle retraction in the proximity of the nucleus (Figure 6k). The desmosomes from the blister region were free floating in the extracellular space in the proximity of their adjacent cells, indicating their detachment from the IFs (Figure 6l).

Tuft1-KO mouse KCs show abnormal differentiation and cytoplasmic DSP accumulation

KO mouse KCs show significant downregulation of loricrin and involucrin, two late-stage differentiation markers (Tharakan et al., 2010) predominantly expressed in the upper suprabasal layers of the epidermis (Figure 6m). This suggests abnormalities within the differentiation processes, as also indicated by the acanthosis observed in the patient's skin and KO mouse skin. For DSP, a significant upregulation was observed in these cells (Figure 6m) with a predominant accumulation in the cytoplasm (Figure 6n). Western blotting of other desmosomal and IF proteins was not significantly affected in TUFT1-deficient mouse KCs (Supplementary Figure S5c), and the desmosome morphometrics were not significantly different (Supplementary Figure S5d). K5 staining showed a slight nuclear retraction, leaving wider gaps between cells (Figure 6n).

TUFT1 KO leads to differential expression of genes involved in epidermal homeostasis

RNA-sequencing analysis on WT and healthy parts of KO skin resulted in 21 significantly differentially expressed genes (false discovery rate < 0.05) (Supplementary Table S4). Thirteen were downregulated, and eight were upregulated. The downregulated genes—*Lep* (Collin et al., 2017), *Serpine1* (Subramaniyam et al., 2010), and *CD36* (Pohl et al., 2005)—are involved in lipid rafts remodeling, a process previously shown to be involved in desmosomes assembly and intercellular adhesion (Resnik et al., 2011). Two upregulated genes, *s100a4* and *K6a*, were previously shown to be involved in hyperkeratotic and inflammatory diseases such as psoriasis (Zibert et al., 2010) and pachyonychia congenita (Forrest et al., 2016). In addition, a publicly available Gene Expression Omnibus dataset showed five genes in a human epidermal injury model, which show the same trendline of expression (upregulation of downregulation) as our KO *Tuft1* murine model (Supplementary Figure S5e).

TUFT1 localizes in the heart at the intercalated discs, but no significant cardiac abnormalities were present in *Tuft1*-KO mice

The hearts of KO mice at age 12 months were not morphometrically different from those of WT (Supplementary Figure S6a). In WT heart tissue, TUFT1 specifically localized at the intercalated discs, similar to the desmosomal proteins DSP and DSC2 (Supplementary Figure S6b), and was absent in KO. No significant differences between WT and KO mice were found on magnetic resonance imaging analysis, showing normal end-systolic/-diastolic volumes, ejection fraction, stroke volume, and systolic/diastolic myomass of the left and right ventricles (Supplementary Figure S6c and d). In addition, mRNA expressions of cardiac injury markers (Eijgenraam et al., 2020) atrial natriuretic peptide gene *Nppa*, brain natriuretic peptide gene *Nppb*, *Myh6*, and *Myh7* were not significantly different between the left and right ventricles of KO mice (Supplementary Figure S6e). In the hearts of WT mice, *Tuft1* mRNA expression levels were 2−4 times lower than the levels in the skin (Supplementary Figure S6f).

Patients' molar does not show any abnormalities

Because TUFT1 was previously suggested to play a role during the development and mineralization of enamel (Deutsch et al., 1991), we investigated the lower right deciduous second molar tooth of one of the patients. Microcomputed tomography scan did not reveal any peculiar features regarding metrics or morphology. Although there was some localized surface enamel demineralization and pitting hypoplasia, there was no evidence of any generalized structural or maturational enamel defects (Supplementary Figure S7a, b, and f). Investigation of four histological ground sections showed a neonatal line in the enamel that was normally positioned and of normal thickness (Supplementary Figure S7c−i).

DISCUSSION

Desmosomes are essential cell−cell connecting structures in different stress-bearing tissues, particularly, in the skin and heart (Green and Simpson, 2007). In this study, we identified TUFT1 as a desmosome-associated component, localizing at the DSP−IF interface of the inner dense plaque. Similar to other desmosomal proteins, TUFT1 expression in cultured KCs is calcium dependent. In addition, its localization is dependent on the DSP C-terminal domain. In a previous yeast two-hybrid study (Paine et al., 1998), TUFT1 was suggested to interact with K5/6, two epidermal expressed proteins that connect to the desmosome. More recently, TUFT1 was identified among several proteins possibly associated with the desmosome in a mass spectrometry analysis using DSP C-terminal and N-terminal constructs as baits (Badu-Nkansah and Lechler, 2020).

Using homozygosity mapping and whole-exome sequencing, a disease-causing splice variant in the *TUFT1* gene, leading to aberrant splicing and a frameshift with loss of protein, was identified in two affected children with skin fragility, WH, and palmoplantar keratoderma. Very recently, biallelic loss-of-function *TUFT1* variants were identified in nine other patients with WH and skin fragility (Jackson et al., 2023). Our study demonstrates that loss of TUFT1 leads to abnormalities in desmosomal morphology, weakened cell−cell contacts, reduced stress resilience of the cell−cell connection, and differentiation disturbances (Wan et al., 2004). In addition, our functional data show that loss of TUFT1 causes desmosome−IF connection defects in patient-derived KCs and directly places TUFT1 within the inner dense plaque of the desmosome. Moreover, we show that *Tuft1* KO in mice reveals a phenotype strikingly similar to that in humans and that the cardiac tissue seems to be spared despite expression of TUFT1 in it.

In contrast to mouse KOs for the plakoglobin gene *Jup* (Bierkamp et al., 1996), *Dsp* (Vasioukhin et al., 2001), *Pkp1* (Rietscher, 2018) and *Dsg1* (Kugelmann et al., 2019), *Tuft1* KOs are compatible with life. All KO mice showed abnormal fur with a wavy appearance mimicking the WH observed in

the patients. In addition, 40% of KO mice developed spontaneous erosions, with disturbed KC cell−cell contacts and impaired IF insertion to the desmosome. The fact that not all mice developed a skin fragility phenotype may depend on the mildness of the skin fragility phenotype, also described by Jackson et al. (2023), as a phenotypic characteristic in most of the affected patients but not present in all.

Despite TUFT1 expression at the intercalated discs of myocardium, no apparent cardiac phenotype was observed in the TUFT1-negative patients (at the ages of 17 and 19 years) nor in the *Tuft1*-KO mice until the age of 12 months. However, cardiac involvement cannot be completely ruled out at this point because no patients aged >23 years have ever been cardiologically evaluated (Jackson et al., 2023). Additional studies are necessary to get more insight into whether TUFT1 plays a role in cardiac function.

Previously, TUFT1 was identified as being involved in the process of enamel mineralization (Deutsch et al., 1991). However, histological analysis of a patient's deciduous molar did not show any abnormalities in enamel or dentine formation. TUFT1 has also been reported to be involved in processes such as chondrogenesis (Sliz et al., 2017) and tumorigenesis (Dou et al., 2019; Liu et al., 2019, 2018; Zhou et al., 2016) and in addition was shown to have a more widespread distribution with likely tissue dependent functions (Leiser et al., 2007). Whether TUFT1 is a structural or a regulatory protein for the desmosome is not clear at the moment, but it does not seem to be essential for desmosome formation or embryonic development of tissues such as skin or heart. Nevertheless, lack of TUFT1 clearly affects desmosomal function and cell−cell connection. Pathogenic variants in other desmosomal genes, such as *DSP*, may cause a variety of phenotypes, involving either skin or heart or both. Whether different pathogenic variants in *TUFT1* may result in a variety of phenotypic effects cannot be determined at the moment. Nonetheless, our data implicate the *TUFT1* gene and its encoding protein in the maintenance of skin integrity and in human monogenetic disease.

In summary, this study identifies TUFT1 as a protein involved in human skin fragility and hair disorders and defines it as a desmosome-associated protein.

MATERIALS AND METHODS

Patients

In the diagnostic setting, clinical photographs, hair samples, skin biopsies, and blood were taken. Written informed consent (University Medical Centre Groningen, Groningen, The Netherlands) was obtained from the parents to use the left-over clinical material for research purposes and publication. Written informed consent (Erasmus Medical Center Rotterdam, Rotterdam, The Netherlands) was obtained from the parents for publication of the images.

Mice

WT and homozygous *Tuft1*-KO mice (Tuft1$^{tm1a(KOMP)Wtsi}$) in a C57BL/6NTac background were produced by the International Mouse Phenotyping Consortium (Wellcome Trust Sanger Institute, Hinxton, United Kingdom; https://www.mousephenotype.org/data/genes/MGI:109572). The study was approved by the local Animal Ethics Committee (license number AVD199105-01-002). ARRIVE (Animal Research: Reporting of In Vivo Experiments) guidelines (Percie du Sert et al., 2020) were used for reporting this study. Our study comprised both a group of mice aged 3 months and a group aged 12 months.

Data availability statement

Additional materials and methods are added as a supplement. RNA-sequencing data can be accessed at the Gene Expression Omnibus database with GSE237986. Nanotomy images can be accessed at www.nanotomy.org.

ORCIDs

Annemieke J. M. H. Verkerk: http://orcid.org/0000-0002-7523-3656
Daniela Andrei: http://orcid.org/0000-0003-4211-2783
Mathilde C. S. C. Vermeer: http://orcid.org/0000-0001-8513-2296
Duco Kramer: http://orcid.org/0000-0003-2091-8436
Marloes Schouten: http://orcid.org/0000-0001-9568-5345
Pascal Arp: http://orcid.org/0009-0004-4227-9510
Joost A. M. Verlouw: http://orcid.org/0000-0003-2373-0981
Hendri H. Pas: http://orcid.org/0000-0001-8823-2591
Hillegonda J. Meijer: http://orcid.org/0000-0003-2567-5031
Marije van der Molen: http://orcid.org/0000-0003-0466-347X
Silke Oberdorf-Maass: http://orcid.org/0009-0002-2382-2034
Miranda.Nijenhuis: http://orcid.org/0000-0002-4212-6926
Pedro H. Romero-Herrera: http://orcid.org/0000-0002-7438-9288
Martijn F. Hoes: http://orcid.org/0000-0002-0234-438X
Jeroen Bremer: http://orcid.org/0000-0002-7550-6386
Johan A. Slotman: http://orcid.org/0000-0001-9705-9620
Peter C. van den Akker: http://orcid.org/0000-0002-3734-753X
Gilles F. H. Diercks: http://orcid.org/0000-0001-8053-216X
Ben N. G. Giepmans: http://orcid.org/0000-0001-5105-5915
Hans Stoop: http://orcid.org/0000-0002-2475-6991
Jasper J. Saris: http://orcid.org/0000-0001-9232-267X
Ans M.W. van den Ouweland: http://orcid.org/0000-0003-2855-6775
Rob Willemsen: http://orcid.org/0000-0002-0443-619X
Jean-Jacques Hublin: http://orcid.org/0000-0001-6283-8114
M. Christopher Dean: http://orcid.org/0000-0003-3783-7296
A. Jeannette M. Hoogeboom: http://orcid.org/0000-0002-5900-567X
Herman H.W. Silljé: http://orcid.org/0000-0003-3292-6302
André G. Uitterlinden: http://orcid.org/0000-0002-7276-3387
Peter van der Meer: http://orcid.org/0000-0002-9705-4413
Maria C. Bolling: http://orcid.org/0000-0003-2086-9363

CONFLICT OF INTEREST

PvdM received consultancy fees and/or grants from Novartis, Pharmacosmos, Vifor Pharma, Astra Zeneca, Pfizer, Abbott, Pharma Nord, Novo Nordisk, BridgeBio, and Ionis, all paid to the institute. The remaining authors state no conflict of interest.

ACKNOWLEDGMENTS

MCB is the guarantor for this work.

The authors thank the family and especially the children for their continuous cooperation, endless patience, perseverance, and trust. The authors acknowledge the late A.P. Oranje for his many years of dedicated supervision of the family. The authors thank Joke Polak and Nicole van Koetsveld for fibroblast cell culture; Lida Prins-Bakker and Lies-Anne Severijnen for experimental and technical support; the late Michael Davidson and Michelle Baird from the United States for cloning fluorescent constructs; and Suzanne Pasmans, Senada Koljenović, Max Kros, and Alice Brooks for fruitful discussions. The authors thank Inge Bruins for her experimental contributions during her thesis. The authors thank Stichting Vlinderkind for the financial support to perform the studies.

Part of the work has been performed in the University Medical Centre Groningen Microscopy and Imaging Center, sponsored by ZonMW grant 91111.006 and the Netherlands Electron Microscopy Infrastructure (NWO 184.034.014).

AUTHOR CONTRIBUTIONS

Conceptualization: AJMHV, DA, PvdM, MCB; Data Curation: DA, JAMV; Formal Analysis: DA, AJMHV, MCSCV, DK, PA, JAMV, MCB; Funding Acquisition: AGU, PvdM, MCB; Investigation: DA, AJMHV, MCSCV, DK, MS, PA, HJM, MvdM, SO-M, MN, PHR-H, JAS, GFHD, HS, JS, MCD, AJMHV; Methodology: AJMHV, DA, DK, MFH, JB, PCvdA, HHWS, PvdM, MCB; Project Administration: AJMHV, PvdM, MCB; Resources: AJMHV, JB, JAS, BNGG, J-JH, AJMH, HHWS, AGU, PvdM, MCB; Supervision: AJMHV, HHP, JB, PvdM, MCB; Validation: PA, MFH, AMWvdO, PvdM, MCB; Visualization: DA, AJMHV; Writing − Original Draft Preparation: AJMHV, DA, MCD, MCB; Writing − Review and Editing: AJMHV, DA, MCSCV, DK, MS, PA, JAMV, HHP,

HJM, MvdM, SO-M, MN, PHR-H, MFH, JB, JAS, PCvdA, GFHD, BNGG, HS, JS, AMWvdO, RW, J-JH, MCD, AJMH, HHWS, AGU, PvdM, MCB

SUPPLEMENTARY MATERIAL

Supplementary material is linked to the online version of the paper at www.jidonline.org, and at https://doi.org/10.1016/j.jid.2023.02.044.

REFERENCES

Badu-Nkansah K, Lechler T. Proteomic analysis of the desmosome identifies novel components required for skin integrity. Mol Biol Cell 2020;31:1140–53.

Beffagna G, de Bortoli M, Nava A, Salamon M, Lorenzon A, Zaccolo M, et al. Missense mutations in Desmocollin-2 N-terminus, associated with arrhythmogenic right ventricular cardiomyopathy, affect intracellular localization of desmocollin-2 in vitro. BMC Med Genet 2007;8:65.

Bierkamp C, Mclaughlin KJ, Schwarz H, Huber O, Kemler R. Embryonic heart and skin defects in mice lacking plakoglobin. Dev Biol 1996;180:780–5.

Brown SDM, Moore MW. The International Mouse Phenotyping Consortium: past and future perspectives on mouse phenotyping. Mamm Genome 2012;23:632–40.

Collin A, Noacco A, Talvas J, Caldefie-Chézet F, Vasson MP, Farges MC. Enhancement of lytic activity by leptin is independent from lipid rafts in murine primary splenocytes. J Cell Physiol 2017;232:101–9.

Deutsch D, Palmon A, Fisher LW, Kolodny N, Termine JD, Young MF. Sequencing of bovine enamelin ("tuftelin") a novel acidic enamel protein. J Biol Chem 1991;266:16021–8.

Dou C, Zhou Z, Xu Q, Liu Z, Zeng Y, Wang Y, et al. Hypoxia-induced TUFT1 promotes the growth and metastasis of hepatocellular carcinoma by activating the Ca2+/PI3K/AKT pathway [published correction appeared in Oncogene 2022;37:4330–4332]. Oncogene 2019;38:1239–55.

Eijgenraam TR, Boukens BJ, Boogerd CJ, Schouten EM, van de Kolk CWA, Stege NM, et al. The phospholamban p. pathogenic variant leads to cardiomyopathy with heart failure and is unresponsive to standard heart failure therapy [published correction appears in Sci Rep 2020;10:16710]. Sci Rep 2020;10:9819.

Forrest CE, Casey G, Mordaunt DA, Thompson EM, Gordon L. Pachyonychia congenita: a spectrum of KRT6a mutations in Australian patients. Pediatr Dermatol 2016;33:337–42.

Gehmlich K, Syrris P, Peskett E, Evans A, Ehler E, Asimaki A, et al. Mechanistic insights into arrhythmogenic right ventricular cardiomyopathy caused by desmocollin-2 mutations. Cardiovasc Res 2011;90:77–87.

Green KJ, Simpson CL. Desmosomes: new perspectives on a classic. J Invest Dermatol 2007;127:2499–515.

Hartlieb E, Kempf B, Partilla M, Vigh B, Spindler V, Waschke J. Desmoglein 2 is less important than desmoglein 3 for keratinocyte cohesion. PLoS One 2013;8:e53739.

Has C, Bauer JW, Bodemer C, Bolling MC, Bruckner-Tuderman L, Diem A, et al. Consensus reclassification of inherited epidermolysis bullosa and other disorders with skin fragility. Br J Dermatol 2020;183:614–27.

Jackson A, Moss C, Chandler KE, Balboa PL, Bageta ML, Petrof G, et al. Biallelic TUFT1 variants cause woolly hair, superficial skin fragility and desmosomal defects. Br J Dermatol 2023;188:75–83.

Jonkman MF, Pasmooij AMG, Pasmans SGMA, van den Berg MP, ter Horst HJ, Timmer A, et al. Loss of desmoplakin tail causes lethal acantholytic epidermolysis bullosa. Am J Hum Genet 2005;77:653–60.

Kugelmann D, Radeva MY, Spindler V, Waschke J. Desmoglein 1 deficiency causes lethal skin blistering. J Invest Dermatol 2019;139:1596–9.e2.

Lee JYW, McGrath JA. Mutations in genes encoding desmosomal proteins: spectrum of cutaneous and extracutaneous abnormalities. Br J Dermatol 2021;184:596–605.

Leiser Y, Blumenfeld A, Haze A, Dafni L, Taylor AL, Rosenfeld E, et al. Localization, quantification, and characterization of tuftelin in soft tissues. Anat Rec (Hoboken) 2007;290:449–54.

Lek M, Karczewski KJ, Minikel EVv, Samocha KE, Banks E, Fennell T, et al. Analysis of protein-coding genetic variation in 60,706 humans. Nature 2016;536:285–91.

Liu H, Zhu J, Mao Z, Zhang G, Hu X, Chen F. Tuft1 promotes thyroid carcinoma cell invasion and proliferation and suppresses apoptosis through the Akt-mTOR/GSK3β signaling pathway. Am J Transl Res 2018;10:4376–84.

Liu W, Chen G, Sun L, Zhang Y, Han J, Dai Y, et al. TUFT1 promotes triple negative breast cancer metastasis, stemness, and chemoresistance by up-regulating the Rac1/β-catenin pathway. Front Oncol 2019;9:617.

McKoy G, Protonotarios N, Crosby A, Tsatsopoulou A, Anastasakis A, Coonar A, et al. Identification of a deletion in plakoglobin in arrhythmogenic right ventricular cardiomyopathy with palmoplantar keratoderma and woolly hair (Naxos disease). Lancet 2000;355:2119–24.

Najor NA. Desmosomes in human disease. Annu Rev Pathol 2018;13:51–70.

Nekrasova O, Green KJ. Desmosome assembly and dynamics. Trends Cell Biol 2013;23:537–46.

Noensie EN, Dietz HC. A strategy for disease gene identification through nonsense-mediated mRNA decay inhibition. Nat Biotechnol 2001;19:434–9.

Norgett EE, Hatsell SJ, Carvajal-Huerta L, Cabezas JC, Common J, Purkis PE, et al. Recessive mutation in desmoplakin disrupts desmoplakin-intermediate filament interactions and causes dilated cardiomyopathy, woolly hair and keratoderma. Hum Mol Genet 2000;9:2761–6.

Obland GF. The fine structure of the interrelationship of cells in the human epidermis. J Biophys Biochem Cytol 1958;4:529–38.

Paine CT, Paine ML, Snead ML. Identification of tuftelin-and amelogenin-interacting proteins using the yeast two-hybrid system. Connect Tissue Res 1998;38:257–67;discussion 295–303.

Percie du Sert N, Hurst V, Ahluwalia A, Alam S, Avey MT, Baker M, et al. The ARRIVE guidelines 2.0: updated guidelines for reporting animal research. PLoS Biol 2020;18:e3000410.

Pohl J, Ring A, Korkmaz U, Ehehalt R, Stremmel W. FAT/CD36-mediated long-chain fatty acid uptake in adipocytes requires plasma membrane rafts. Mol Biol Cell 2005;16:24–31.

Quinlan RA, Schwarz N, Windoffer R, Richardson C, Hawkins T, Broussard JA, et al. A rim-and-spoke hypothesis to explain the biomechanical roles for cytoplasmic intermediate filament networks. J Cell Sci 2017;130:3437–45.

Resnik N, Sepčić K, Plemenitaš A, Windoffer R, Leube R, Veranič P. Desmosome assembly and cell-cell adhesion are membrane raft-dependent processes. J Biol Chem 2011;286:1499–507.

Rietscher K. Regulation of PKP1's function in intercellular adhesion, proliferation and barrier formation. thesis. Martin Luther University, Halle-Wittenberg; 2018. https://docslib.org/doc/5786348/regulation-of-pkp1%C2%B4s-function-in-intercellular-adhesion-proliferation-and-barrier-formation (accessed November 6, 2023).

Schweingruber C, Rufener SC, Zünd D, Yamashita A, Mühlemann O. Nonsense-mediated mRNA decay — mechanisms of substrate mRNA recognition and degradation in mammalian cells. Biochim Biophys Acta 2013;1829:612–23.

Simpson CL, Kojima S, Cooper-Whitehair V, Getsios S, Green KJ. Plakoglobin rescues adhesive defects induced by ectodomain truncation of the desmosomal cadherin desmoglein 1: implications for exfoliative toxin-mediated skin blistering. Am J Pathol 2010;177:2921–37.

Sliz E, Taipale M, Welling M, Skarp S, Alaraudanjoki V, Ignatius J, et al. TUFT1, a novel candidate gene for metatarsophalangeal osteoarthritis, plays a role in chondrogenesis on a calcium-related pathway. PLoS One 2017;12:e0175474.

Stahley SN, Bartle EI, Atkinson CE, Kowalczyk AP, Mattheyses AL. Molecular organization of the desmosome as revealed by direct stochastic optical reconstruction microscopy. J Cell Sci 2016;129:2897–904.

Subramaniyam D, Zhou H, Liang M, Welte T, Mahadeva R, Janciauskiene S. Cholesterol rich lipid raft microdomains are gateway for acute phase protein, SERPINA1. Int J Biochem Cell Biol 2010;42:1562–70.

Takeichi T, Liu L, Fong K, Ozoemena L, McMillan JR, Salam A, et al. Whole-exome sequencing improves mutation detection in a diagnostic epidermolysis bullosa laboratory. Br J Dermatol 2015;172:94–100.

Tharakan S, Pontiggia L, Biedermann T, Böttcher-Haberzeth S, Schiestl C, Reichmann E, et al. Transglutaminases, involucrin, and loricrin as markers of epidermal differentiation in skin substitutes derived from human sweat gland cells. Pediatr Surg Int 2010;26:71–7.

Vasioukhin V, Bowers E, Bauer C, Degenstein L, Fuchs E. Desmoplakin is essential in epidermal sheet formation. Nat Cell Biol 2001;3:1076–85.

Vermeer MCSC, Andrei D, Marsili L, van Tintelen JP, Silljé HHW, van den Berg MP, et al. Towards a better understanding of genotype–phenotype correlations and therapeutic targets for cardiocutaneous genes: the importance of functional studies above prediction. Int J Mol Sci 2022;23:10765.

Wan H, Dopping-Hepenstal PJC, Gratian MJ, Stone MG, Zhu G, Purkis PE, et al. Striate palmoplantar keratoderma arising from desmoplakin and desmoglein 1 mutations is associated with contrasting perturbations of desmosomes and the keratin filament network. Br J Dermatol 2004;150:878–91.

Watt FM, Mattey DL, Garrod DR. Calcium-induced reorganization of desmosomal components in cultured human keratinocytes. J Cell Biol 1984;99:2211–5.

Xu J, Ma H, Liu Y. Stochastic optical reconstruction microscopy (STORM). Curr Protoc Cytom 2017;81:12–46. 1–12.46.27.

Zhang MQ. Statistical features of human exons and their flanking regions. Hum Mol Genet 1998;7:919–32.

Zhou B, Zhan H, Tin L, Liu S, Xu J, Dong Y, et al. TUFT1 regulates metastasis of pancreatic cancer through HIF1-Snail pathway induced epithelial-mesenchymal transition. Cancer Lett 2016;382:11–20.

Zibert JR, Skov L, Thyssen JP, Jacobsen GK, Grigorian M. Significance of the S100A4 protein in psoriasis. J Invest Dermatol 2010;130:150–60.

SUPPLEMENTARY MATERIALS AND METHODS

SNP array analysis

DNA of the two affected children was investigated by Affymetrix SNP array 6.0 analysis for copy-number variations in Nexus (BioDiscovery, El Segundo, CA). No large deletions or amplifications were present. Fourteen, large homozygous regions were detected in the DNA of both affected siblings indicating a consanguineous relationship in the parents. Fourteen homozygous areas >1 Mb were shared by the children (indicated in Supplementary Table S1). The largest region was 7.59 Mb on chromosome 1 (chr1:144.438.562-152.024.771, build 37). None of the recessive or dominant genes known to be involved in woolly hair syndrome or epidermolysis bullosa simplex diseases were located in any of the shared homozygous areas.

Whole-exome sequencing

Genomic DNA from whole blood was fragmented into 200−400 bp fragments using Covaris Adaptive Focused Acoustics shearing according to the manufacturer's instructions (Covaris, Woburn, MA). Illumina TruSeq DNA library preparation (Illumina, San Diego, CA) was performed on a Caliper SciClone NGS workstation (Caliper Life Sciences, Hopkinton, MA), followed by exome capture using a NimbleGen SeqCap EZ V2 kit (Roche Nimblegen, Madison, WI). This capture targets 44 Mb of exonic regions covering 30,246 coding genes, 329,028 exons, and 710 microRNAs. Paired-end sequencing (2 × 100 bp) was performed at six samples per lane using Illumina TruSeq V3 chemistry on a HiSeq2000 (Illumina), with a total amount of at least 4 Gb per sample. Data processing and variant calling were done according to an optimized version of the Genome Analysis Tool Kit (Broad Institute, Cambridge, MA) (McKenna et al., 2010). Variant annotation on final VCF (Variant Call Format) files was performed by an in-house developed pipeline, adapted, and extended from the Annovar tool (Wang et al., 2010), including functional annotation, database frequencies, pathogenicity risk scores, and conservation predictions as well as gene coupled phenotypes. The exomes of the two affected children and their father were sequenced with a mean coverage for the separate samples of 54× (II2), 61× (II1), and 90× (I1). Variants were filtered on the basis of recessive mode of inheritance, impact on protein function, and frequency <0.0001 in public databases. One variant, in the *TUFT1* gene, located on chromosome 1 remained in the total of homozygous areas indicated in Supplementary Table S2.

Variant pathogenicity prediction

Pathogenicity of exome-sequence variants and its impact on protein function were predicted by programs integrated into the Annovar tool (Wang et al., 2010). Splice-site variant prediction analysis was performed with Alamut variant interpretation Software, version 2.7.2 (SOPHiA GENETICS, Lausanne, Switzerland) and consisted of SpliceSiteFinder-like, MaxEntScan, NNSPLICE, and GeneSplicer.

Sanger sequencing

To confirm the mutation found by whole exome sequencing, Sanger sequencing was performed by BaseClear B.V. (Leiden, The Netherlands). Primers used to generate PCR products and mutation validation by Sanger Sequencing are indicated in Supplementary Table S8.

RT-PCR on RNA from blood

Primers used to generate RT-PCR fragments and/or used for sequencing are indicated in Supplementary Tables S8 and S9. RT-PCR fragments were electrophoretically separated using the Labchip GX system (PerkinElmer, Waltham, MA). Sanger sequencing of the RT-PCR products was performed and repeated three times (at BaseClear B.V.).

Nonsense-mediated mRNA decay inhibition

Patient- and control- derived fibroblast cells were cultured at 37 °C and 5% carbon dioxide in HAM's (F10 + 15% fetal calf serum + 1% penicillin/streptomycin). For the nonsense-mediated mRNA decay inhibition test cells were incubated with 50 µl of cycloheximide (50 mg/ml) in a T75 culture flask containing 10 ml medium for 4.5 hours. cDNA was made with 500 ng RNA using the RT-qPCR protocol of the Maxima H Minus First Strand cDNA Synthesis kit with dsDNAse (Thermo Fisher Scientific, Waltham, MA). Relative *TUFT1* mRNA expression levels were determined with qRT-PCR using *TUFT1* and *EMC7* (reference gene) primers and probes (Thermo Fisher Scientific; TUFT1:hs01064711_m1; EMC7:hs00220077_m1), both with primers spanning exon junctions. This experiment was performed in triplo using three different dilutions. A paired *t*-test was used for statistical analysis of Ct values.

Keratinocytes isolation and culture

Human keratinocytes were isolated as previously described (Jonkman et al., 1997) from biopsies (patients) or redundant healthy skin obtained from breast reduction surgery (control). Keratinocytes were grown and passaged in serum-free medium (CtP, CELLnTEC, Bern, Switzerland) until about 80% confluent. Before switching to high-calcium medium, cells were incubated for 24 hours with CtP-2D (CELLnTEC, Bern, Switzerland). After 24 hours, the medium was replaced with high-calcium (1.2 mM) CtP-2D media supplemented with 5 µg/ml gentamycin (Thermo Fisher Scientific, Waltham, MA) and 1.25 µg/ml amphotericin B (Thermo Fisher Scientific). The period of high-calcium exposure is described for each experiment.

Mouse keratinocytes were isolated from adult mice tails (the group aged 3 months), as previously described (Li et al., 2017). Briefly, after trypsinization, cells were filtered through 100 µm cell strainers (Falcon, Corning, Tewksbury, MA) and centrifuged for 10 minutes at 300*g*. The supernatant was removed, and the cells were resuspended in EpiLife medium (Thermo Fisher Scientific) supplemented with EpiLife Defined Growth Supplement (Thermo Fisher Scientific). Cells were plated at 1−2 × 10^5 cells/ml density on coated (coating matrix protein; Thermo Fisher Scientific) stretchable plates (Bioflex; plates collagen I) for the purpose of enhancing adhesion to the culture surface. When cells became approximately 80% confluent, media was replaced with 1.2 mM calcium-containing medium. HaCaT cells were cultured in DMEM (Thermo Fisher Scientific) supplemented with 5% fetal calf serum, 1% glutamine, 100 U/ml penicillin, and 100 µg/ml streptomycin.

Immunofluorescence and light microscopy

Both human and mouse skin biopsies were snap frozen, sliced into 4 μm sections on a microtome, and immunofluorescent stained as previously described (Jonkman et al., 1992). Cultured human or mouse keratinocytes were grown in their specific media containing 1.2 mM calcium for 2 days. For immunofluorescence staining, cells were fixed with 2% formaldehyde in PBS for 10 minutes, air dried, and frozen. Permeabilization was performed with 0.5% Triton X-100 in PBS for 5 minutes at room temperature. Nonspecific staining was blocked by incubation with 1% ovalbumin for 20 minutes, followed by primary antibody incubation for 60 minutes at 37 °C and 30 minutes with a secondary antibody. Cells were mounted with SlowFade DAPI (Thermo Fisher Scientific). Imaging was conducted with the Leica DFC350FX camera (Leica, Wetzlar, Germany) mounted on a LEICA DMRA microscope supported by LAS-software (Leica). Antibodies used are listed in Supplementary Table S5.

For the triple immunofluorescence staining from Supplementary Figure S4a, images were scanned with the Leica SP8X confocal microscope.

Snap-frozen skin and cultured keratinocytes were stained with H&E for morphology assessment. Likewise the immunofluorescence staining, the human primary keratinocytes were grown in media containing 1.2 mM calcium for 2 days, fixed with 2% formaldehyde for 10 minutes, air dried, and frozen until stained with H&E. The extracellular area of the H&E-stained cultured keratinocytes was calculated by measuring the cells area and subtracting it from the whole picture area. The area in pixels was corrected for area in micrometers. An unpaired *t*-test was used for statistical analysis.

Gel electrophoresis and western blotting

For western blotting experiments, human primary and mouse keratinocytes were isolated as described earlier. The human keratinocytes were exposed to high calcium (1.2 mM) for 5 days (owing to the highest TUFT1 expression) (Supplementary Figure S4b), and mouse keratinocytes were exposed for 2 days at 1.2 mM calcium (owing to their shorter lifespan in culture).

Proteins were extracted from cultured keratinocytes using a buffer containing 62 mM Tris-hydrogen chloride, 2.5% SDS, and 1 mM EDTA; protease inhibitor (Roche, Indianapolis, Indiana, USA); phosphatase inhibitor cocktail 3 (Sigma-Aldrich, St. Louis, MO, USA); and sodium orthovanadate (Sigma-Aldrich, St. Louis, MO, USA). The total protein amount was quantified using Pierce BCA Protein Assay, and afterward, sample buffer (10% glycerol, 5% β-mercaptoethanol, and bromophenol blue) was added. Proteins were separated in 5 or 10% SDS-PAGE gels and transferred to polyvinylidene fluoride membranes. The membranes were incubated overnight at 4 °C with primary antibody, followed by secondary antibody (horse radish peroxidase–labeled) incubation for 1 hour at room temperature. The images were acquired using ImageQuant LAS software. On the basis of normality, statistics were performed using unpaired *t*-test/Mann–Whitney test. Antibodies used are listed in Supplementary Table S5.

Keratinocyte dissociation assay

For this experiment, we used patient and control primary keratinocytes. Cells were grown in 12-well plates in CtP medium to 100% confluency. Four additional days after they became confluent, the medium was changed with CtP- 2D. On day 5, CtP- 2D medium was replaced with CtP- 2D medium containing 1.2 mM calcium, and on day 6, a keratinocyte dissociation assay was performed. Briefly, the cells were washed with Hanks' Balanced Salt Solution and incubated with 400 μl dispase (2.4 U/ml) (Thermo Fisher Scientific, Waltham, MA) at 37 °C. To extend the end-diameter of the pipet tips, we cut off 1 cm from the 1 ml pipet tips. Tips were then incubated in 1% BSA solution (Merck KGa, Darmstadt, Germany) for at least 15 minutes prior to the experiment to avoid adherence when pipetting. After the cell layers detached completely, the sheaths were washed with Hanks' Balanced Salt Solution, and the layers were resuspended 10 times with the 1 ml special-cut tips. Formaldehyde was added to preserve the sheaths and crystal violet for the coloration (Merck KGa). After 24 hours, pictures were taken.

Direct stochastic optical reconstruction microscopy

Human primary keratinocytes were grown on 24 mm ø 1.5 H cover glasses (Paul Marienfeld, Lauda-Königshofen, Germany) for 7 days with high calcium and immunostained as described earlier. TUFT1 was labeled in combination with desmoglein 3 or the rod domain of desmoplakin I followed by Alexa 647–conjugated goat anti-rabbit IgG and Atto 488–conjugated goat anti-mouse Fab-fragments. Imaging was performed on a Zeiss Elyra microscope (Zeiss, Jena, Germany) using a 100× 1.46 numerical aperture plan-apo lens as described previously (Slotman et al., 2020). In short, imaging was performed in low-oxygen buffer using high laser-power fluorophores forced into a dark state. Subsequently, a movie was made under similar conditions where each fluorophore that exited the dark state and thus emitted photons was detected and localized by Gaussian fitting using the Zeiss Zen software (Zeiss, Jena, Germany). Images were constructed by plotting a two-dimensional Gaussian on each detected molecule with a width based on the detection precision. Antibodies used are listed in Supplementary Table S6.

Electron microscopy and nanotomy

Human and mouse keratinocytes were grown on Bioflex plates with their specific media until 50% confluent and then switched to 1.2 mM calcium-containing media for 2 days and then fixated with 2% glutaraldehyde (Merck, Burlington, CA) in 0.1 M cacodylate buffer (Sigma Aldrich, Steinheim, Germany). Mouse and human skin biopsies or keratinocytes were fixed with 2% glutaraldehyde in 0.1 M cacodylate buffer at pH 7.4. After fixation, samples were postfixed with 1% osmium tetroxide (EMS, Hatfield, PA, USA)/1.5% potassium ferrocyanide (Merck) (2 hours at 4 °C) and then dehydrated using ethanol and embedded in EPON epoxy resin (Serva, Heidelberg, Germany) (Vermeer et al., 2021). Sections (80 nm) were cut transverse to cell direction and contrasted using 2% uranylacetate (Merck) in water for 45 minutes. Images of desmosomes were taken with CM100 TEM microscope (FEI, Hillboro, OR). Nanotomy-scanned samples were imaged as previously described (Sokol et al., 2015) and can be accessed under www.nanotomy.org.

Pre-embedding immunolabeling for electron microscopy

Human primary keratinocytes were grown for 4 days on high calcium in Lab-TekII (Thermo Fisher Scientific) chamber slides. After short formalin fixation, 0.05% Triton-X100 permeabilization, and 1% hydrogen peroxide quenching, the cells were incubated with tuftelin antibody (N3C3), followed by horse radish peroxidase–conjugated IgG. The gold substituted Silver intensified diaminobenzidine protocol of Görcs et al. (1986) was used. Antibodies used are listed in Supplementary Table S7.

RNA sequencing

Total RNA was isolated from mouse snap-frozen whole skin, as described earlier for RT-PCR. The QuantSeq 3′ mRNA kit (Lexogen, Vienna, Austria) was used to prepare cDNA sequence libraries. Libraries were sequenced at 2 × 150 bp on a NextSeq 500 sequencer (Illumina). Raw sequence reads were aligned to the mm39 mouse reference genome using STAR (version 2.7.9a) (Dobin et al., 2013) using basic two-pass mode. Duplicate reads were marked using the Genome Analysis Toolkit (version 4.2.4.0) (McKenna et al., 2010). Reads were counted per exon in the GENCODE, version M30, mouse gene annotation using featureCounts (subread version 2.0.3) (Liao et al., 2014). Count file was subset per tissue type and analyzed using edgeR (version 3.36.0), filtering on expression in at least three samples and transcript count of at least one count per million reads. Normalization was performed using the trimmed mean of m-values methodology. Differential expression was determined on knockouts over controls, and false discovery rate < 0.05 differentially expressed genes were extracted. Pathway enrichment was performed by hand on the basis of the Kyoto Encyclopedia of Genes and Genomes and Gene Ontology databases.

RT-PCR on heart tissue

Total RNA from keratinocytes, skin, and heart was isolated. Briefly, snap-frozen organs were powdered and lysed in TRIzol (Sigma-Aldrich, St. Louis, MO) using TissueLyser (Qiagen, Hilden, Germany). cDNA was synthesized by reverse transcription (Qiagen, Hilden, Germany), and real-time quantitative PCRs were performed using SYBR Green (Bio-Rad Laboratories, Hercules, CA). Primers used are listed in Supplementary Table S10. Relative expression was calculated using the ddCt method (Livak and Schmittgen, 2001), and statistics were performed on dCt results using unpaired *t*-test/Mann–Whitney test on the basis of normality.

HaCaT transfection with fluorescent constructs

Immortalized human keratinocytes (HaCaT) were 80–90% confluent at the time of transfection and cotransfected with desmoglein 2–mCherry/keratin 14–mApple, and TUFT1–C-GFP in a ratio of 6:2 Lipofectamine2000:DNA. Cells were fixated with 2% formaldehyde and mounted with SlowFade. Imaging was conducted with the Leica DFC350FX camera mounted on a LEICA DMRA microscope supported by LAS software.

Masson's trichrome staining for mice heart

Transverse mice heart (the group aged 12 months) sections were dehydrated, paraffin embedded (Klinipath, Duiven, The Netherlands), and cut into 4-μm thick sections. Masson's trichrome staining was performed as previously described (Borgdorff et al., 2012) to detect collagen accumulation as a measurement of fibrosis.

Cardiac magnetic resonance imaging

Cardiac magnetic resonance imaging measurements were performed for mice group aged 12 months using an AVANCE 400 MR system (Bruker BioSpin, Ettlingen, Germany) as previously described (Bartelds et al., 2011). Volumetric analyses were performed using cvi42 software (version 5.10.1, Circle Cardiovascular Imaging, Calgary, Canada).

Tooth investigation

The lower right deciduous second molar tooth of one of the patients was extracted for clinical reasons, independently from this research, and donated for study with consent. To study enamel development, formation rate, and thickness in detail, four histological ground sections were made. An extensive description of the materials and methods can be found in the supplementary data tooth analysis file.

Statistics

All data are represented as means ± SEM. For all data, a Shapiro–Wilk normality test was performed. If data were normally distributed, a *t*-test was performed, and if the data were not normally distributed, a Mann–Whitney test was performed. A $P < 0.05$ was considered statistically significant. For qPCR, the dCt values were used for statistical analysis, and 2^{-DDCT} was used for graphical representation. For western blotting, relative expression (protein/housekeeping protein) was used for statistical analysis, and the fold change was used for graphical representations. Statistics were performed using GraphPad Prism (GraphPad Software, San Diego, CA).

SUPPLEMENTARY REFERENCES

Bartelds B, Borgdorff MA, Smit-van Oosten A, Takens J, Boersma B, Nederhoff MG, et al. Differential responses of the right ventricle to abnormal loading conditions in mice: pressure vs. volume load. Eur J Heart Fail 2011;13:1275–82.

Borgdorff MAJ, Bartelds B, Dickinson MG, Boersma B, Weij M, Zandvoort A, et al. Sildenafil enhances systolic adaptation, but does not prevent diastolic dysfunction, in the pressure-loaded right ventricle. Eur J Heart Fail 2012;14:1067–74.

Dobin A, Davis CA, Schlesinger F, Drenkow J, Zaleski C, Jha S, et al. STAR: ultrafast universal RNA-seq aligner. Bioinformatics 2013;29:15–21.

Görcs TJ, Léránth C, MacLusky NJ. The use of gold-substituted silver-intensified diaminobenzidine (DAB) and non-intensified DAB for simultaneous electron microscopic immunoperoxidase labeling of tyrosine hydroxylase and glutamic acid decarboxylase immunoreactivity in the rat medial preoptic area. J Histochem Cytochem 1986;34:1439–47.

Jonkman MF, de Jong MCJM, Heeres K, Sonnenberg A. Expression of integrin alpha 6 beta 4 in junctional epidermolysis bullosa. J Invest Dermatol 1992;99:489–96.

Jonkman MF, Scheffer H, Stulp R, Pas HH, Nijenhuis M, Heeres K, et al. Revertant mosaicism in epidermolysis bullosa caused by mitotic gene conversion. Cell 1997;88:543–51.

Li F, Adase CA, Zhang LJ. Isolation and culture of primary mouse keratinocytes from neonatal and adult mouse skin. J Vis Exp 2017;125:e56027.

Liao Y, Smyth GK, Shi W. featureCounts: an efficient general purpose program for assigning sequence reads to genomic features. Bioinformatics 2014;30:923–30.

Livak KJ, Schmittgen TD. Analysis of relative gene expression data using real-time quantitative PCR and the 2−ΔΔCT method. Methods 2001;25:402–8.

McKenna A, Hanna M, Banks E, Sivachenko A, Cibulskis K, Kernytsky A, et al. The Genome Analysis Toolkit: A MapReduce framework for analyzing next-generation DNA sequencing data. Genome Res 2010;20:1297–303.

Slotman JA, Paul MW, Carofiglio F, de Gruiter HM, Vergroesen T, Koornneef L, et al. Super-resolution imaging of RAD51 and DMC1 in DNA repair foci reveals dynamic distribution patterns in meiotic prophase. PLoS Genet 2020;16:e1008595.

Sokol E, Kramer D, Diercks GFH, Kuipers J, Jonkman MF, Pas HH, et al. Large-scale electron microscopy maps of patient skin and mucosa provide insight into pathogenesis of blistering diseases. J Invest Dermatol 2015;135:1763–70.

Vermeer MCSC, Bolling MC, Bliley JM, Arevalo Gomez KFA, Pavez-Giani MG, Kramer D, et al. Gain-of-function mutation in ubiquitin ligase KLHL24 causes desmin degradation and dilatation in hiPSC-derived engineered heart tissues. J Clin Invest 2021;131:e140615.

Wang K, Li M, Hakonarson H. ANNOVAR: functional annotation of genetic variants from high-throughput sequencing data. Nucleic Acids Res 2010;38:e164.

a

```
CAGGAGATACAGGTGGTGCTAGAAAAGCCAAATGGCTTTAGTCAGAGTCCCACAGCCCTG ex 5/6
TACAGCAGCCCACCTGAGGTGGACACCTGTATAAATGAGGATGTTGAGAGCTTGAGGAAG ex 7
ACGGTGCAGGACTTGCTGGCCAAGCTTCAGGAGGCCAAGCGGCAACACCAGTCAGACTGT ex 7
GTGGCTTTTGAGGTCACACTCAGCCGGTACCAGAGGGAAGCAGAACAAAGTAATGTGGCC ex 8
CTTCAGAGAGAGGAGGACAGAGTGGAGCAGAAAGAGGCAGAAGTCGGAGAGCTGCAGAGG ex 8
CGCTTGCTAGGGATGGAGACGATTTTCTTTTGTGGCCCACCCGGGAGCATCAGGCCTTAC ex 8/intr 8/ex 9
TGGCGAAAGTGAGGGAAGGGGAGGTGGCCCTAGAGGAACTTCGGAGCAACAATGCTGACT ex 9
GCCAAGCAGAACGAGAAAAGGCTGCTACCCTGGAAAAGGAAGTGGCCGGGTTGCGGGAGA ex 10
AGATCCACCACTTGGATGACATGCTCAAGAGCCAGCAGCGGAAAGTCCGGCAAATGATAG ex 10
AGCAGCTCCAGAATTCAAAAGCTGTGATCCAGTCAAAGGACGCCACCATCCAGGAGCTCA ex 11
AGGAG
```

b

```
 1a MNGTRNWCTLVDVHPEDQAAGSVDILRLTLQGELTGDELEHIAQKAGRKTYAMVSSHSAG ex1/ex2/ex3
  b MNGTRNWCTLVDVHPEDQAAGSVDILRLTLQGELTGDELEHIAQKAGRKTYAMVSSHSAG ex1/ex2/ex3
  c MNGTRNWCTLVDVHPEDQAAGSVDILRLTLQGELTGDELEHIAQKAGRKTYAMVSSHSAG ex1/ex2/ex3

 61a HSLASELVESHDGHEEIIKVYLKGRSGDKMIHEKNINQLKSEVQYIQEARNCLQKLREDI ex3/ex4/ex5
  b HSLASELVESHDGHEEIIKVYLKGRSGDKMIHEKNINQLKSEVQYIQEARNCLQKLREDI ex3/ex4/ex5
  c HSLASELVESHDGHEEIIKVYLKGRSGDKMIHEKNINQLKSEVQYIQEARNCLQKLREDI ex3/ex4/ex5

121a SSKLDRNLGDSLHRQEIQVVLEKPNGFSQSPTALYSSPPEVDTCINEDVESLRKTVQDLL ex5/ex6/ex7
  b SSKLDRNLGDSLHRQEIQVVLEKPNGFSQSPTALYSSPPEVDTCINEDVESLRKTVQDLL ex5/ex6/ex7
  c SSKLDRNLGDSLHRQEIQVVLEKPNGFSQSPTALYSSPPEVDTCINEDVESLRKTVQDLL ex5/ex6/ex7

181a AKLQEAKRQHQSDCVAFEVTLSRYQREAEQSNVALQREEDRVEQKEAEVGELQRRLLGME ex7/ex8
  b AKLQEAKRQHQSDCVAFEVTLSRYQREAEQSNVALQREEDRVEQKEAEVGELQRRLLGME ex7/ex8
  c AKLQEAKRQHQSDCVAFEVTLSRYQREAEQSNVALQREEDRVEQKEAEVGELQRRLLGME ex7/ex8

241a TEHQALLAKVREGEVALEELRSNNADCQAERE KAATLEKEVAGLREKIHHLDDMLKSQQR ex9/ex10
  b TGCYPGKGSGRVAGEDPPLG*STOP                                     ex8/ex10
  c TIFFCGPPGSIRPYWRK*STOP                                       ex8/intron8/ex9

301a KVRQMIEQLQNSKAVIQSKDATIQELKEKIAYLEAENLEMHDRMEHLIEKQISHGNFSTQ ex10/ex11/ex12
  b
  c

361a   ARAKTENPGSIRISKPPSPKPMPVIRVVET                               ex12/ex13
  b
  c
```

Supplementary Figure S1. Aberrant TUFT1 cDNA and (deduced) protein sequences. (**a**) cDNA sequence present in patients, with the last 23 bp of intron 8 retained (in pink, with c.724-2A>G splice variant in bold and underlined) and including exon 9. The different exons are indicated in different colors. Primers used for RT-PCR are indicated in turquoise (outer primers), and primers for sequencing are underlined (inner primers) and indicated in Supplementary Table S9. The alternative acceptor splice site that is used is the AG sequence in intron 8 at position c.724-24_25 directly preceding the region indicated in pink. Use of this alternative splice site is also predicted by four splice-site analysis programs incorporated in Alamut (version 2.7.2) when there is a loss of the original acceptor splice site. (**b**) Normal and deduced mutated TUFT1 protein with 1a: normal TUFT1 protein; NP_064512; 1b: deduced protein without exon 9 (*p.Glu242Glyfs*20*); and 1c: deduced protein retaining 23 bp of intron 8 + exon 9 (*p.Glu242Ilefs*17*). Exons (abbreviated as ex) are alternately colored. Orange amino acids indicate codons bridging introns.

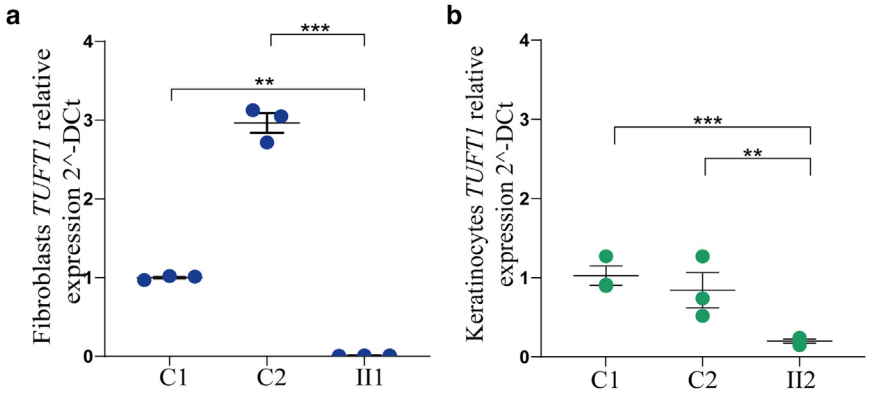

Supplementary Figure S2. *TUFT1* mRNA levels. (**a**) *TUFT1* baseline mRNA expression levels in fibroblasts cultured from two different healthy donors (C1 and C2) and patient II1, detected by qPCR. Error bar = SEM; data were analyzed with unpaired *t*-test. $^{**}P < 0.005$ and $^{***}P < 0.0005$. Ct average: C1 = 29.8; C2 = 27.9; and II1 = 36.2. (**b**) *TUFT1* baseline mRNA expression levels in keratinocytes cultured in 5 days of high Ca2+ from two different healthy donors (C1 and C2) and patient II2, detected by qPCR. Error bar = SEM; data were analyzed with unpaired *t*-test. $^{**}P < 0.005$ and $^{***}P < 0.0005$. Ct average: C1 = 29.0; C2 = 29.4; and II2 = 32.3. Ca^{2+}, calcium.

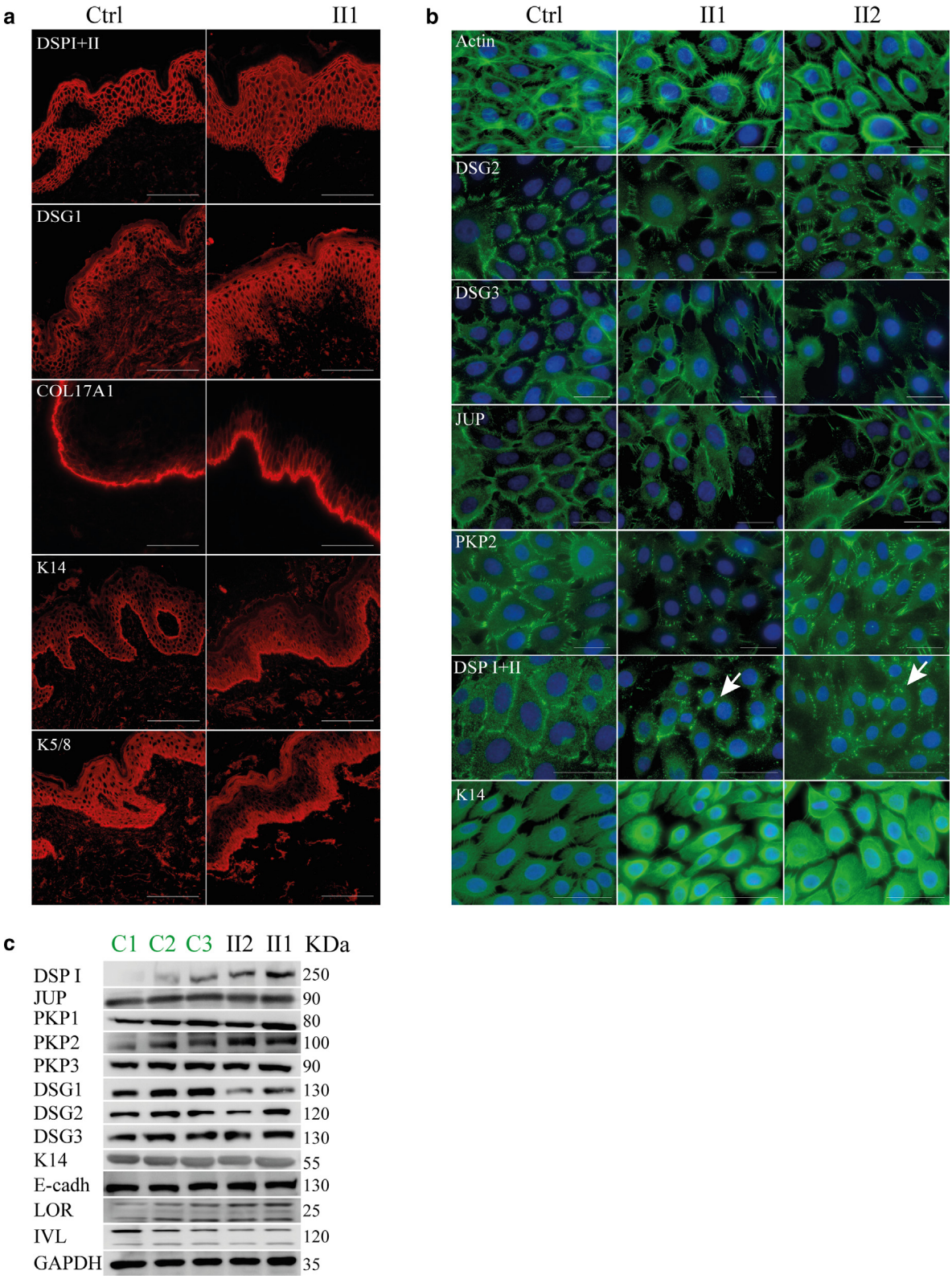

Supplementary Figure S3. Patients' skin and keratinocytes characterization. (**a**) Additional immunofluorescence staining of the whole skin does not indicate reduction or upregulation of the indicated proteins in patient II1. Bar = 50 μm. (**b**) Immunofluorescence staining of cultured primary patient and Ctrl keratinocytes. Arrows indicate a disturbed and more focal distribution of desmoplakin along the cell borders in the patients. Bar = 50 μm. **(c)** Keratinocyte protein extracts analyzed for the indicated proteins by western blot. C1, C2, and C3 denote Ctrl keratinocytes derived from different donors. II1 and II2 denote patients' keratinocytes. Antibodies are listed in Supplementary Table S5. DSPI+II denotes desmoplakin, a combination of two different antibodies. Ctrl, control; DSG, desmoglein; E-cad, E-cadherin 1; IVL, involucrin; JUP, plakoglobin; K, keratin; LOR, loricrin.

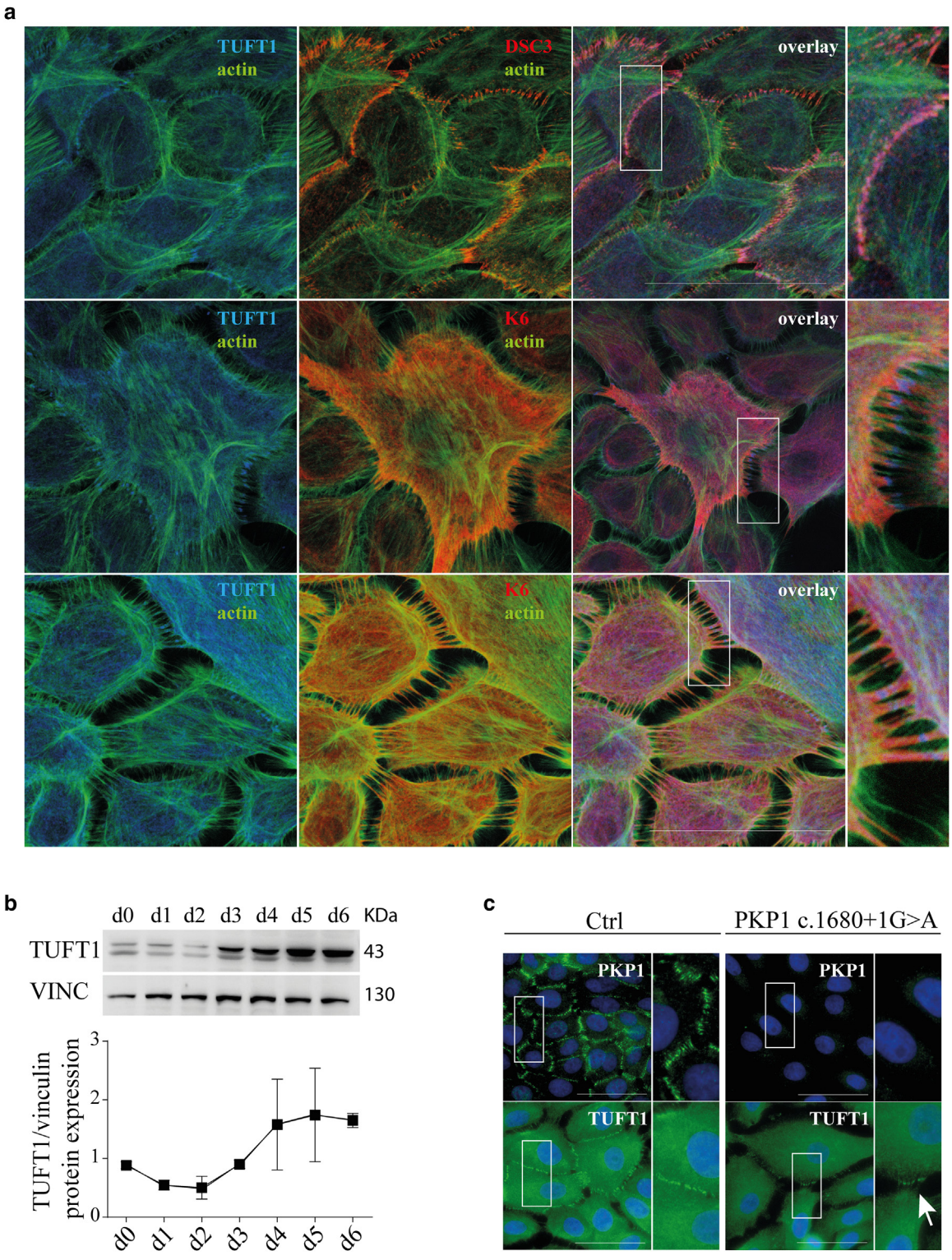

Supplementary Figure S4. TUFT1 localization and expression in human keratinocytes. **(a)** Immunofluorescence triple staining of cultured control primary keratinocytes. Magnified areas, indicated with white boxes, are shown in the last column. Bar = 50 μm. Antibodies are listed in Supplementary Table S5. **(b)** TUFT1 protein expression in keratinocytes cultured in low calcium (d0) and several days (d1−d6) in high Ca2+. VINC was used as a reference protein. n = 3. Error bars = SEM. **(c)** Homozygous *PKP1*-deficient human primary keratinocytes (c.1680+1G>A). Immunofluorescence staining for PKP1 (upper panels) and TUFT1 (lower panels) were performed. Ca^{2+}, calcium; d, day; DSC, desmocollin; K, keratin; VINC, vinculin.

Supplementary Figure S5. Additional *Tuft1*-KO mice hair and skin analysis. **(a)** Scanning electron microscopy of mouse hairs. Knockout mice hair showed a groove-like shape (arrows) compared with the flattened cylinder shape of WT hair. Bar = 20 μm. n = 2 WT; n = 2 KO. **(b)** Mouse snap-frozen skin immunofluorescent staining for the indicated proteins. TUFT1 was stained with both human/mouse-specific antibodies (N3C3/Pac8). Nonspecific staining of N3C3 TUFT1 (human) antibody persists, especially on the basement membrane of homozygous KO mice. Antibodies are listed in Supplementary Table S5. **(c)** Western blot showing the presence of different desmosomal proteins in cultured WT and KO mice keratinocytes. n = 4 WT; n = 6 KO. Protein quantification is shown in the graph on the right, as fold change expression. Antibodies are listed in Supplementary Table S5. **(d)** EM images of mice WT and KO cultured keratinocytes. Morphometrics of the desmosome lengths and interdesmosomal distance are shown in the graphs on the right (not significantly different). **(e)** GO datasets (GDS4608) for an epidermal injury human model show the same pattern of expression as our RNAseq results for five of the genes. *K6A* and *LHX2* are upregulated in the injured skin (also upregulated in *Tuft1*-KO mice skin), and *TUFT1*, *NPR3*, and *DGAT2* show downregulation in the injured epidermis (also downregulated in the murine KO skin). Error bars = SEM. Complete RNAseq gene expression from *Tuft1* KO is shown in Supplementary Table S4. Ctrl, control; DSG, desmoglein; EM, electron microscopy; GO, Gene Ontology; K, keratin; KO, knockout; PLEC, plectin; PPL, periplakin; RNAseq, RNA sequencing; WT, wild-type.

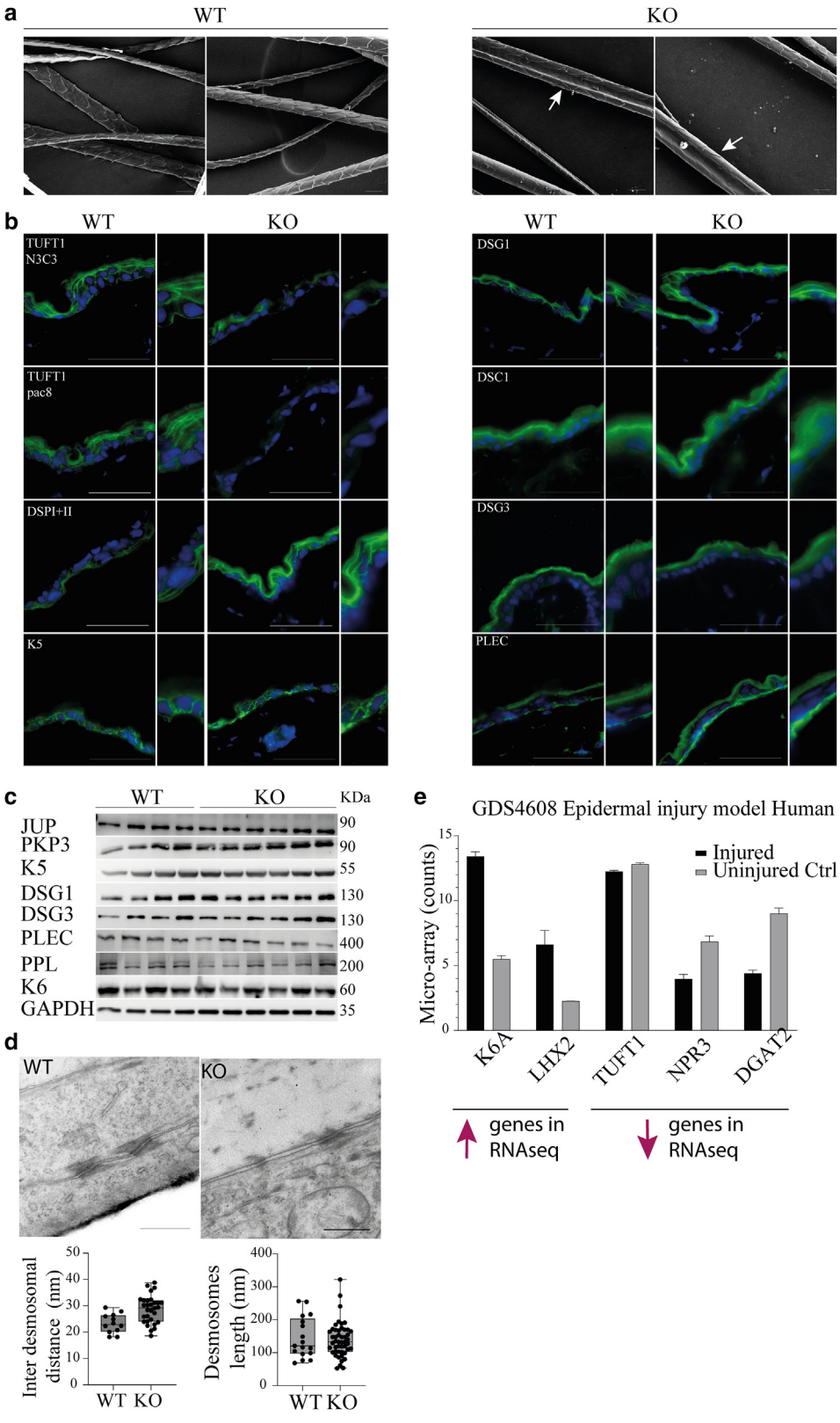

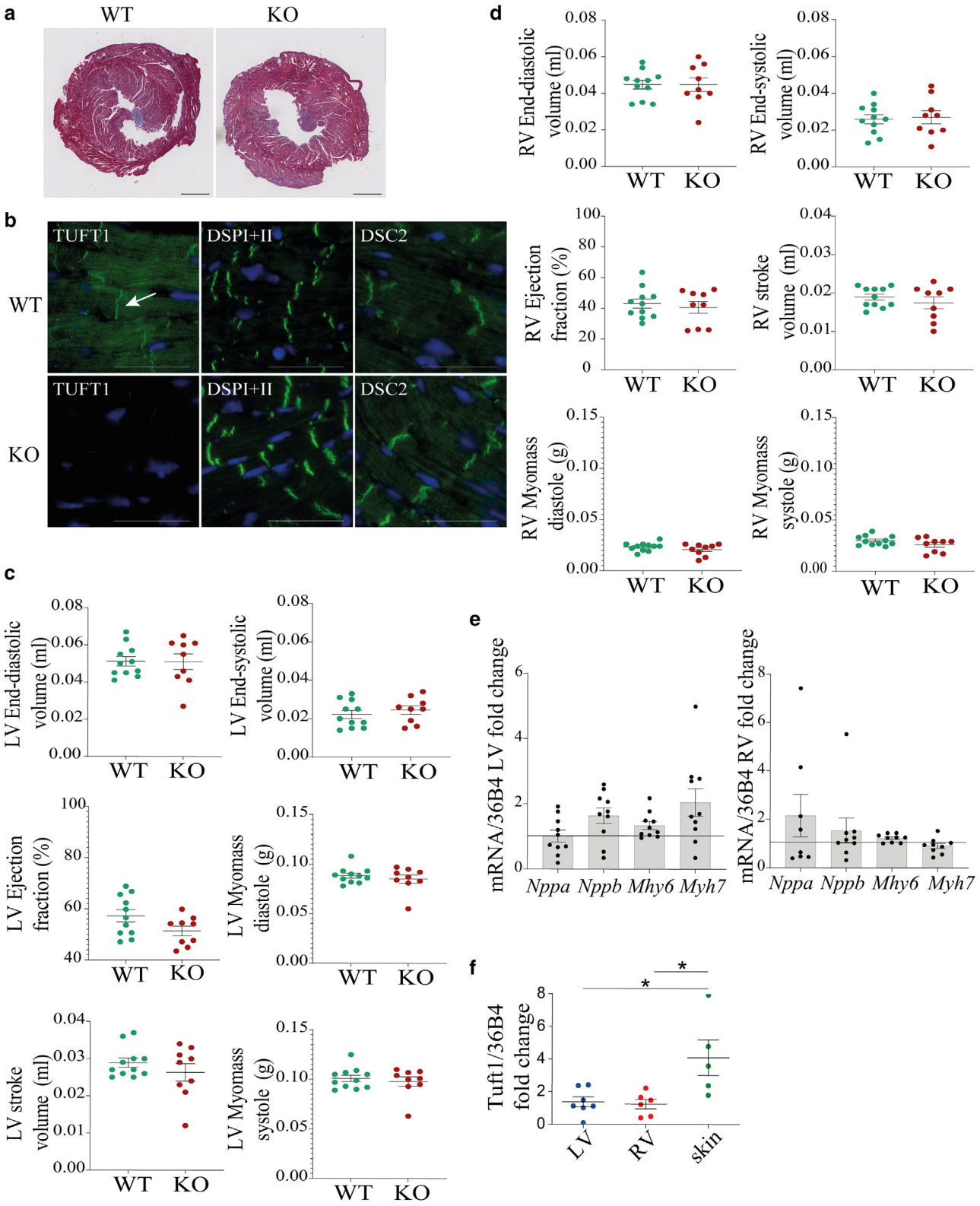

Supplementary Figure S6. Cardiac examination of *Tuft1*-KO mice aged 12 months. (**a**) Masson trichrome staining of the LV heart tissue shows no difference between WT and KO mice. **(b)** Immunofluorescent staining of *Tuft1*, *Dsp*, and *Dsc2* (green) in LV. Bar = 50 μm. Antibodies are listed in Supplementary Table S5. **(c, d)** Graphic representation of MRI cardiac analysis of *Tuft1*-KO mice and WT mice aged 12 months. ESV, EDV, EF, SV, and systolic/diastolic myomass were analyzed for the (**c**) LV and the (**d**) RV. n = 11 WT; n = 9 KO. **(e)** qPCR measurements of left/right ventricular mRNA levels of heart failure markers: atrial natriuretic peptide gene *Nppa*, brain natriuretic peptide gene *Nppb*, *Myh6*, and *Myh7*. n = 9 WT; n = 10 KO. **(f)** Comparison of *Tuft1* gene expression measured by qPCR in LV, RV, and skin derived from WT mice. $*P < 0.05$. Average Ct values: LV = 34.4, RV = 34.2, skin = 35.5. DSP, desmoplakin; EDV, end-diastolic volume; EF, ejection fraction; ESV, end-systolic volume; KO, knockout; LV, left ventricle; MRI, magnetic resonance imaging; RV, right ventricle; SV, stroke volume; WT, wild-type.

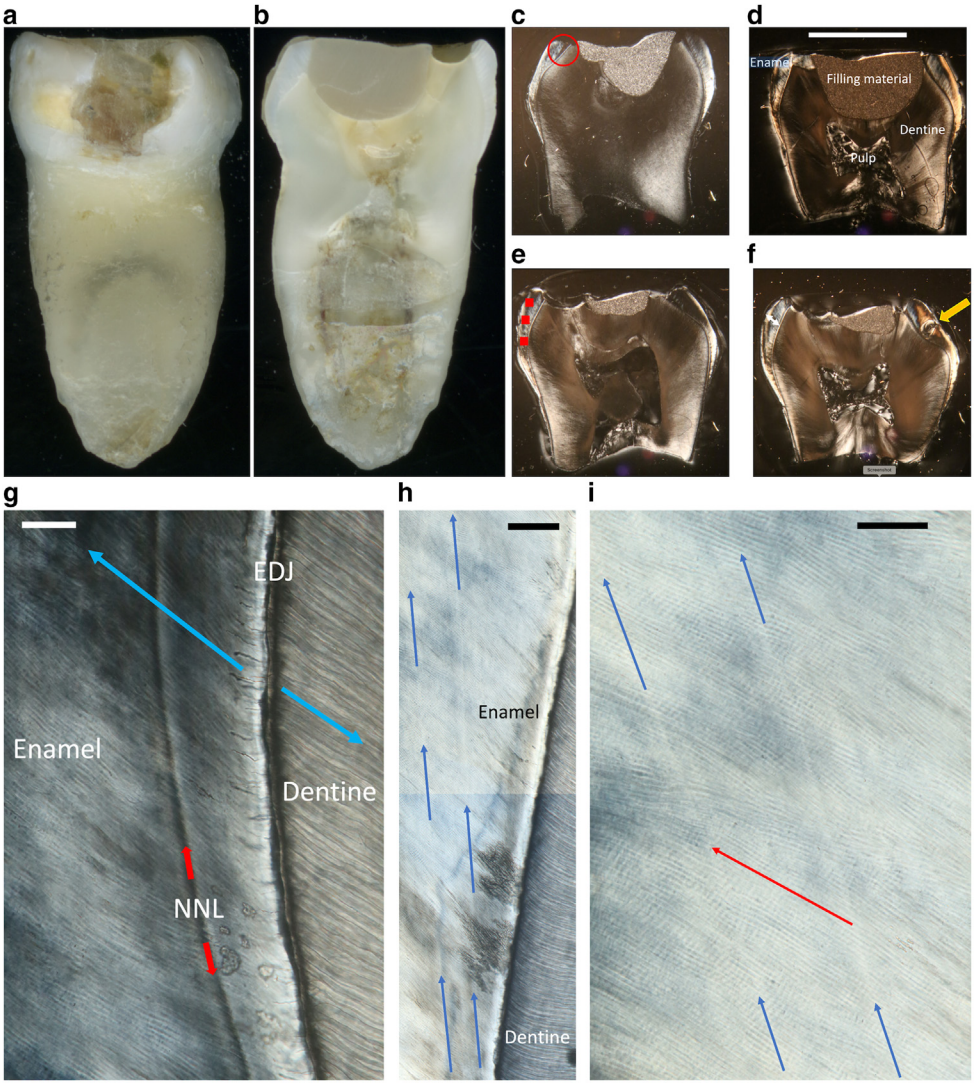

Supplementary Figure S7. Patient tooth analysis. (**a**) Distal aspect of the lower right deciduous second molar tooth (maximum tooth crown width = 8 mm), **(b)** polished block face cut longitudinally through the distal cusps, and **(c–f)** serial longitudinal ground sections of the enamel crown (bar = 4 mm) showing the occlusal restoration and active caries on the distal aspect of the crown. The red circle in **c** indicates the position of the NNL that is imaged at higher power in **g**; red squares in **e** indicate the approximate positions of measurements used to estimate rates of enamel formation. The lower red square is in inner enamel, the middle is in mid-enamel, and the top is in outer enamel. The central pulp cavity, dentine core of the tooth, enamel cap, and glass ionomer filing material are indicated in **d**. Double white arrow in **f** indicates the position where linear enamel thickness was measured; yellow arrow indicates an enamel lesion confluent with a surface pit where some demineralization around the periphery of the cavity is present. **(g)** Polarized transmitted light micrograph (×25 objective, bar = 40 μm) of the NNL indicated by red arrows in enamel to the left of the EDJ. Enamel is secreted away from the EDJ during tooth development to the left, whereas dentine is secreted away from the EDJ to the right, each indicated by blue arrows. **(h)** Section of the enamel shown in **e**; the blue arrows indicate two bright diverging accentuated markings that correspond to DKTP vaccinations given 4 weeks (28 days) apart (bar = 100 μm). **(i)** Polarized transmitted light micrograph (×25 objective, bar = 50 μm) in the same region showing the two bright diverging accentuated markings (blue arrows). The red arrow lies along the path of the enamel prisms (or rods) that make up the fine structure of enamel. These run from the EDJ toward the enamel surface in the direction of the red arrow. Along each prism, small daily increments of enamel growth are demarcated by alternating dark and light markings. These enable rates of enamel formation to be estimated as described in the supplementary data tooth analysis file. EDJ, enamel dentine junction; NNL, neonatal line.

Supplementary Table S1. Overlapping Homozygous Regions >1 Mb in the Affected Children II1 and II2

Chromosome	Start	End	Length Region
1q21.2	144 438 562	152 024 771	7.59 Mb
2q11.2	94 705 115	97 347 414	2.64 Mb
3p21.2	50 497 815	52 019 922	1.52 Mb
3p12.2	82 581 121	84 377 841	1.8 Mb
3q12.1	97 537 665	98 837 901	1.3 Mb
4p15.1	32 459 479	34 399 050	1.94 Mb
7q11.21	62 188 256	63 336 521	1.15 Mb
8q13.1	67 572 694	68 691 207	1.12 Mb
10p12.31	21 611 872	22 819 036	1.42 Mb
12p11.21	33 531 025	37 330 729	3.80 Mb
14q23.3	65 953 506	66 967 438	1.02 Mb
16p11.2	32 017 826	34 783 983	2,77 Mb
16q22.1	65 563 933	67 247 446	1,68 Mb
18q11.2	16 100 000	17 563 228	1,46 Mb

Positions are in Build 37.

Supplementary Table S2. Flow Scheme of Exome Sequencing Variant Filtering

Filtering Steps	Number of Variants
Total number of variants	39,952
recessive model	1,225
exonic, splicing	818
without synonymous	392
freq in ExAc <0.0001	6
freq in ESP <0.0001	4
freq in RSX2 <0.0001	2
not in dbSNP	2
in homozygous area	1

Supplementary Table S3. Genelist Used as Reference for Variant Detection in Woolly Hair and Skin Fragility Phenotypes

Gene	Protein	Protein Type	Chr. Location	Inheritance	Associated Syndrome	Skin Phenotype	Hands and/or Feet	Nails	Hair Phenotype	Heart Phenotype	OMIM
Including hair phenotype											
LIPH	Lipase H	Triglyceride lipase	3q27.2	AR	—	—	—	—	Woolly hair, hypotrichosis	None	[1]607365
LPAR6	Lysophosphatidic acid receptor	G-protein coupled receptor	13q14.2	AR	—	—	—	—	Woolly hair, hypotrichosis	None	[1]609239
K25	Keratin 25	Keratin, type I (acidic)	17q21.2	AR	—	—	—	—	Woolly hair	None	[1]616646
K74	Keratin 74	Keratin, type II (neutral)	12q13.13	AD, AR	—	—	—	—	Woolly hair, hypotrichosis	None	[1]608248
K71	Keratin 71	Keratin, type II (neutral)	12q13.13	AD	—	—	—	—	Woolly hair, hypotrichosis	None	[1]608245
KANK2	KN motif ankyrin repeat domain-containing protein 2	SRC-interacting protein	19p13.2	AR	—	—	PKK	—	Woolly hair	None	[1]614610
DSC2	Desmocollin 2	Cadherin, glycoprotein	18q21.1	AD, AR	—	—	Mild PPK	—	Woolly hair	ARVD	[1]125645
DSP	Desmoplakin	Plakin, Anchoring protein	6p24.3	AD, AR	Carvajal syndrome, EBS	Skin fragility	PKK	Yes	Woolly hair, alopecia	ARVD, DCM	[1]125647
JUP	Junction Plakoglobin	Catenin, Armadillo	17q21.2	AD, AR	Naxos disease, EBS	Skin fragility, mild	PKK, diffuse type	Yes	Woolly hair, alopecia	ARVC, arrhythmia	[1]173325
PKP1	PKP1	Catenin, Armadillo	1q32.1	AR	EBS	Skin fragility, ectodermal dysplasia	PPK, blisters	Thickened, dystrophic	Short and sparse	None	[1]601975
KLHL24	Kelch-like family member 24	E3 ubiquitin ligase	3q27.1	AD	EBS	Skin fragility	—	Dystrophic	Hair loss, scalp	None	[1]611295
CDSN	corneodesmosin	Glycoprotein	6p21.33	AD, AR	Peeling skin syndrome	Peeling skin	—	Normal	Hypotrichosis, scalp only	None	[1]602593
DSC3	Desmocollin 3	Cadherin	18q12.1	AR	—	Skin vesicles	—	—	Hypotrichosis	None	[1]600271
DSG1	Desmoglein 1	Cadherin	18q21.1	AD, AR	—	Erythroderma	PKK	—	Hypotrichosis	None	[1]125670
DSG4	Desmoglein 4	Cadherin	18q12.1	AR	—	—	—	—	Hypotrichosis	None	[1]607892
Normal hair phenotype											
EXPH5	Exophilin 5	Synaptotagmin-like	11q22.3	AD, AR	EB, nonspecific	Skin fragility	—	Normal	Normal	None	[1]612878
K5	Keratin 5	Keratin, type II (neutral)	12q13.13	AD	EBS	Skin fragility	PPK	Sometimes	Normal	None	[1]148040

(*continued*)

Supplementary Table S3. Continued

Gene	Protein	Protein Type	Chr. Location	Inheritance	Associated Syndrome	Skin Phenotype	Hands and/or Feet	Nails	Hair Phenotype	Heart Phenotype	OMIM
TGM5	Transglutaminase 5	Catalyzing enzyme	15q15.2	AR	Peeling skin syndrome 2	Blistering, peeling skin	blistering, peeling skin	Normal	Normal	None	[1]603805
K14	Keratin 14	Keratin, type I (acidic)	17q21.2	AD, AR	Dowling-Meara, Weber-Cockayne, EBS	Skin fragility	PPK	Sometimes	Normal or thin straight hair	None	[1]148066
DSG3	Desmoglein 3	Cadherin	18q12.1	AR	—	Oral mucosa blistering	—	—	—	—	[1]169615
Heart only											
PKP2	PKP2	Catenin, Armadillo	12p11.21	AD	—	—	—	—	Normal	ARVD	[1]602861
DSG2	Desmoglein 2	Cadherin	18q12.1	AD	—	—	—	—	Normal	ARVD	[1]125671
No human mutations described											
PKP3	PKP3	Catenin, Armadillo	11p15.5	—	—	—	—	—	—	—	[1]605561
DSC1	Desmocollin 1	Cadherin	18q12.1	—	—	—	—	—	—	—	[1]125643

Abbreviations: AD, autosomal dominant; AR, autosomal recessive; ARVC, right ventricular cardiomyopathy; ARVD, arrhythmogenic right ventricular dysplasia; Chr., chromosome; DCM, dilated myocardiopathy; DSG, desmoglein; EBS, epidermolysis bullosa simplex; JUP, plakoglobin; K, keratin; OMIM, Online Mendelian Inheritance in Man; PKK, palmoplantar keratoderma; SRC, steroid receptor coactivator.
[1]Indicates MIM gene.

Supplementary Table S4. Differential Expression of Genes in Mouse Skin Analyzed by RNAseq

Gene Symbol	Gene Name	Log FC	*P*-Value	FDR
Upregulated in KO				
Defb8	Defensin beta 8	4.43	1.57E-16	2.04E-12
K6a	Keratin 6A	2.32	6.47E-11	4.19E-07
Lhx2	LIM homeobox protein 2	2.18	1.12E-05	1.12E-02
Sdr16c5	Short chain dehydrogenase/reductase family 16C, member 5	1.79	2.35E-05	1.90E-02
Slc27a4	Solute carrier family 27	1.79	9.79E-06	1.06E-02
Cers4	Ceramide synthase 4	1.74	4.45E-05	3.20E-02
Tmem164	Transmembrane protein 164	1.66	7.97E-05	4.92E-02
S100a4	S100 calcium binding protein A4	1.07	6.24E-05	4.25E-02
Downregulated in KO				
Lep	Leptin	−2.39	1.84E-07	5.96E-04
Serpine1	Serine (or cysteine) peptidase inhibitor, clade E, member 1	−2.38	2.98E-05	2.27E-02
Tuft1	TUFT1	−2.1	3.25E-06	3.82E-03
Npr3	Natriuretic peptide receptor 3	−2.06	2.30E-09	9.93E-06
Btg2	BTG anti-proliferation factor 2	−2	1.61E-05	1.49E-02
Hp	Haptoglobin	−1.93	2.48E-06	3.56E-03
Timp4	Tissue inhibitor of metalloproteinase 4	−1.73	7.33E-05	4.75E-02
Plin1	Perilipin 1	−1.53	1.78E-05	1.54E-02
Fabp4	Fatty acid binding protein 4, adipocyte	−1.52	2.91E-06	3.78E-03
Dgat2	Diacylglycerol O-acyltransferase 2	−1.48	3.43E-07	8.89E-04
Adipoq	Adiponectin, C1Q and collagen domain containing	−1.47	7.91E-07	1.64E-03
Lpl	Lipoprotein lipase	−1.42	1.09E-06	1.77E-03
CD36	CD36 molecule	−1.4	8.89E-07	1.64E-03

Abbreviations: FC, fold change; FDR, false discovery rate; KO, knockout; RNAseq, RNA sequencing.

Supplementary Table S5. Antibody List (Immunofluorescence and WB)

Primary Antibody	Host Species	Reactive Species	Dilution Cells	Dilution Cryosection	Dilution WB	Supplier	Catalog Number	Used in
Phalloidin (actin)		488 labeled	1/100			Tebu-bio	PHDG1	Supplementary Figures S3b and S4a
BP180 ectodomain (COL17A1)	Mouse	Human	1/20	1/30			University of Lowa and University of Michigan gift	Supplementary Figure S3a
DSG1	Rabbit	Human		1/1,000	1/1,000	Abcam	ab124798	Supplementary Figures S3c and S5b and c
DSG1	Mouse	Human		1/20		Tebu-bio	sc-59904	Supplementary Figure S3a
DSC3	Mouse	Human	1/2,5	1/5		Progen	65193	Supplementary Figure S4a
DSC1 (NBP1)	Rabbit	Human		1/200		Novus	NBP1-88099	Supplementary Figure S5b and c
DSC2	Rabbit	Human		1/100		Progen	610120	Supplementary Figures S5b and c and S6b
DSG3	Mouse	Human			1/250	Progen	G194	Supplementary Figures S3c and S5c
DSG3	Rabbit	Human	1/400	1/400		Abcam	EPR14101	Supplementary Figures S3b and S5b
DSG2	Mouse	Human	undiluted		1/200	Progen	65159	Supplementary Figure S3b and c
DSPI (2.17)	Mouse	Human	1/100	1/200	1/1,000	MyBioSource	MBS530881	Figure 6m and n and Supplementary Figure S3b and c
DSP I+II (2.15)	Mouse	Human	1/50	1/100		Progen	61003	Supplementary Figure S3a and b
DSP (ab71690)	Rabbit	Human		1/100		Abcam	ab71690	supp. fig. 5b, supp. fig. 6b
Involucrine	Mouse	Human		1/100	1/3,000	Sigma-Aldrich	I9018	Figure 6m and Supplementary Figure S3c
K14	Mouse	Human	1/30	1/20	1/6,000	Dundee	LL001	Supplementary Figures S3a and c and S4a
K14	Mouse	Human	1/10			Dundee	LL002	Supplementary Figure S3b
K5/8	Mouse	Human		1/10		Raemakers	RCK102	Supplementary Figure S3a
K5	Rabbit	Human		1/400	1/5,000	Abcam	ab75869	Supplementary Figure S5c
Loricrin	Rabbit	Human		1/1,200	$^{1}/_{2}$,000	Biolegend	905101	Figure 6m and Supplementary Figure S3c
PKP1	Mouse	Human		1/2	1/300	MyBioSource	MBS531465	Supplementary Figures S3c and S4c
PKP2	Mouse	Human	1/4	1/4	1/50	Progen	651101	Supplementary Figure S3b and c
PKP3	Mouse	Human	1/25	1/50	1/500	Progen	270.6.2	Supplementary Figures S3c and S5c
Plakoglobin	Mouse	Human	1/250	1/1,000	1/5,000	Sigma-Aldrich	P8087	Figure 5d and Supplementary Figures S3b and c and S5c
vinculin	Mouse	Human			1/5,000	Abcam	ab18058	Supplementary Figures S3c and S4b
TUFT1 (Pac8)	Rabbit	Mouse		1/30	1/800	Clone Cloud Co	PAC829Mu01	Figures 6g,h, m and n Supplementary Figures S5b and S6b
TUFT1	Rabbit	Human			1/800	Abcam	ab184949	Figure 2e and Supplementary Figure S4b
TUFT1 (N3C3)	Rabbit	Human	1/100	1/50		GeneTex	GTX115014	Figures 3b, 4a, and 5d and Supplementary Figure S4a and c and Supplementary Figure S5b
K5	Rabbit	Human	1/50	1/200		ITK	905503	Figures 4a and 6n and Supplementary Figure S5b
E-cadherin	Mouse	Human			1/1,000	Thermo Fisher Scientific	NCH-38	Supplementary Figur S3c
Tubulin	Mouse	Human			1/20,000	Sigma-Aldrich	t5168	Supplementary Figure S3c
K6	Mouse	Human	1/10		1/500	Progen	61090	Supplementary Figures S4a and S5b and c
Plectin	Mouse	Human			1/500	Santa Cruz	10F6	Supplementary Figure S5b and c
Periplakin	Goat	Human			1/300	Santa Cruz	sc-16754	Supplementary Figure S5c
GAPDH	Mouse	Human			1/25,000	Fitzgerald	10r-g109a	Figures 2e and 6m and Supplementary Figures S3c and S5c

Secondary Antibody	Host Species	Reactive Species	Label	Dilution	Supplier	Catalog Number	Used in
Goat anti-rabbit	Goat	Rabbit	HRP labeled	WB 1/2,000	Dako/Agilent	P044801	Figures 2e and 6m and Supplementary Figures S3c, S4b, and S5c

(*continued*)

Supplementary Table S5. Continued

Secondary Antibody	Host Species	Reactive Species	Label	Dilution	Supplier	Catalog Number	Used in
Rabbit anti-mouse	Rabbit	Mouse	HRP labeled	WB 1/2,000	Dako	P0260	Figure 2e and 6m and Supplementary Figures S3c, S4b, and S5c
Rabbit anti-goat	Rabbit	Goat	HRP labeled	WB 1/2,000	Dako	P0449	Supplementary Figure S5c
Donkey anti-rabbit FITC	Donkey	Rabbit	FITC	IF cryosection: 1/100	Jackson	711-096-152	Figures 3b and 6g and h and Supplementary Figures S5b and S6b
Goat anti Mouse Alexa 568	Goat	Mouse	Alexa 568	IF cryosection: 1/400	Invitrogen	A-11031	Figure 5d and Supplementary Figure S3a
Goat anti Mouse Alexa 488	Goat	Mouse	Alexa 488	IF cells: 1/600	Molecular Probes	A-11029	Figure 6n and Supplementary Figures S4c and d and S3b
Goat anti-rabbit Alexa 647	Goat	Rabbit	Alexa 647	IF cells: 1/150	Invitrogen	A21245	Supplementary Figure S4a
Goat anti Mouse Alexa 568	Goat	Mouse	Alexa 568	IF cells: 1/300	Invitrogen	A-11031	Supplementary Figure S4a
Goat anti-rabbit FITC	Goat	Rabbit	FITC	IF cells: 1/100	Invitrogen	62-1811	Figures 4a and 5d and Supplementary Figures S3b and S4c
Donkey anti-rabbit RRX	Donkey	Rabbit	LRSC (RXX)	IF cells: 1/300	Jackson ImmunoResearch	711-085-152	Figure 6n

Abbreviations: DSG, desmoglein; DSP, desmoplakin; HRP, horse radish peroxidase; IF, intermediate filament; K, keratin; WB, western blotting.

Supplementary Table S6. dSTORM Superresolution

Antibody	Host Species	Reactive Species	Dilution	Supplier	Catalog Number
Primary					
TUFT1 (N3C3)	Rabbit	Human	1/50	GeneTex	GTX115014
DSPI (2.17)	Mouse	Human	1/100	MyBioSource	MBS530881
desmoglein 3 (5G11)	Mouse	Human	1/30	tebu-bio	sc-53487
Secondary					
Alexa 647 conjugated IgG	Goat	Rabbit	1/200	Invitrogen	A21245
Atto 488	Goat	Mouse	1/200	Hypermol	2112-250UG

Abbreviation: dSTORM, Direct Stochastic Optical Reconstruction Microscopy.

Supplementary Table S7. Immunolabeling Antibodies for Electron Microscopy

Antibody	Host Species	Reactive Species	Dilution	Supplier	Catalog Number
Primary					
TUFT1 (N3C3)	rabbit	human	1/50	GeneTex	GTX115014
Secondary					
Goat-anti-rabbit IgG HRP	goat	rabbit	1/50	ITK (Dako)	P0448

Supplementary Table S8. Primers Used for Mutation Verification in TUFT1 by Sanger Sequencing

Primers	Position	Sequence
For generating PCR products		
fw1 5′−3′	Intron 8	TAGCTGGCGAGTGGGCCTGCAT
rv1 5′−3′	Intron 9	CAGCTTCATGAGGAGATAC
fw2 5′−3′	Intron 8	GTACAGATGCCCCTTTTGAAG
rv2 5′−3′	Intron 9	CTGATGAAAAATGGAATGAGCA
For sequencing of PCR products		
seq-fw 5′−3′	Exon 9	TTACTGGCGAAAGTGAGGGA
seq-rv 5′−3′	Intron 9	AAGAGATACCATTTGGGTCC

Abbreviations: fw, forward; rv, reverse; seq-fw, sequence forward; seq-rv, sequence reverse.

Supplementary Table S9. RT-PCR Primers Spanning TUFT1 Exon 5−11 and Used for RT-PCR and cDNA Sequencing

Primers	Position	Sequences
For generating RT-PCR products		
TFT_F2 5′−3′	Exon 5−6	CAGGAGATACAGGTGGTGC
TFT_R2 5′−3′	Exon 11	CTTGAGCTCCTGGATGGTGG
For sequencing of RT-PCR products		
TFT_F1 5′−3′	Exon 6	ACAGCCCTGTACAGCAGCC
TFT_R1 5′−3′	Exon 11	GATGGTGGCGTCCTTTGAC

Supplementary Table S10. Mouse Primers for RNAseq Validation and Heart Function

Species	Primers Sequence
m36B4-Fw	AAGCGCGTCCTGGCATTGTC
m36B4-Rw	GCAGCCGCAAATGCAGATGG
mu Nppa fw	GCTTCCAGGCCATATTGGAG
mu Nppa rv	GGTGGTCTAGCAGGTTCTTG
mu Nppb fw	CTCCTATCCTCTGGGAAGTC
mu Nppb rv	CCGATCCGGTCTATCTTGTG
mu Myh6 fw	AGCTCATGGCTACACTCTTC
mu Myh6 rv	GTGGGTGGTCTTCAGGTTTG
mu Myh7 fw	GAGCATTCTCCTGCTGTTTC
mu Myh7 rv	GAGCCTTGGATTCTCAAACG

Abbreviations: fw, forward; mu, murine; RNAseq, RNA sequencing; rv, reverse.